Università degli Studi di Padova

Dipartimento di Fisica e Astronomia "Galileo Galilei"
Corso di Laurea Magistrale in Fisica

Study of the EFILE diagnostic under radiofrequency electric field

Relatore:
Dr. Gianluigi Serianni
Correlatrice:
Dr. Laurence Cherigier-Kovacic

Laureando:
Carlo Poggi
Matricola 1127982

Anno Accademico 2016/2017

Abstract

The electric field is a parameter of special relevance in plasma physics. Its fluctuations are responsible for various macroscopic phenomena, such as anomalous transport in fusion plasmas or plasma-wall interactions, and its measure is therefore required.

At present, most diagnostic tools perturb the field (like Langmuir probes) or require multiple simultaneous measures to achieve a good spatial resolution (like spectroscopy and tomography).

The EFILE diagnostic (Electric Field Induced Lyman-α Emission) is currently under development at PIIM laboratory at Aix-Marseille Université (France) and aims to provide a non intrusive and precise measurement of the electric field in the plasma edge region, using a beam of hydrogen atoms prepared in the metastable $2s$ state. The metastable particles are obtained by means of a proton beam extracted from a hydrogen plasma source, and neutralised by interaction with vaporised caesium. When a $2s$ atom enters a region where an electric field is present, it undergoes a transition to the $2p$ state (*Stark mixing*). It then quickly decays to the ground level, emitting Lyman-α radiation, which is collected by a photomultiplier. The $2s \rightarrow 2p$ transition rate is proportional to the square of the magnitude of the electric field, and depends on the field oscillation frequency (with peaks around 1 GHz). By measuring the intensity of the Lyman-α radiation emitted by the beam it is possible to determine the magnitude of the field in a defined region.

In this work, an analysis of the behaviour of the diagnostic under static or radiofrequency electric field is presented. Electric field simulations obtained with a finite element solver of Maxwell equations, combined with theoretical calculations of the Stark mixing transition rate, are used to develop a model for the interpretation of photomultiplier data. This method shows good agreement with experimental results for the static field case, and allows to measure the field magnitude for the oscillating case. Issues linked to the experimental set-up and limits of the diagnostic itself are shown and possible design implementations are given.

Contents

Chapter 1

Introduction

1.1 The energetic problem

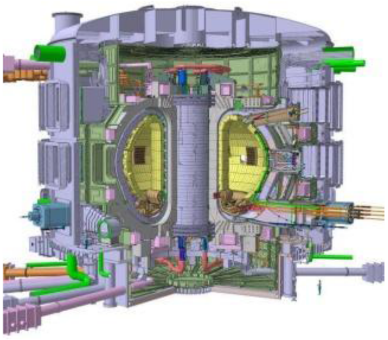

Figure 1.1: The ITER reactor.

During last years the per capita energy consumption has grown considerably, as a consequence of globalisation and the fast technological development, which acted as a catalyst for the industrial development. The exploitation of the energetic resources has increased as well, dramatically reducing the amount of non-renewable energy reserves. The research for alternative energy resources seems therefore mandatory for a society willing to further progress.

The ITER project (International Thermonuclear Experimental Reactor) moves in this direction: the aim is to realise a thermonuclear reactor, with a Tokamak configuration, using fusion reactions between the hydrogen isotopes deuterium and tritium to produce more energy than that needed to run the machine. This will be achieved by magnetically confining a plasma, heated at a temperature of about 20 keV [16]. ITER is currently under construction in Cadarache (France).

1.2 Measuring the electric field in plasmas

A plasma consists of negatively and positively charged particles, showing a collective behaviour [3]. Its evolution is described by the laws of magneto-hydrodynamics: the dynamics of charged particles is intimately connected to the electromagnetic field, and perturbations of charge and current densities give rise to variations of $\vec{E}$ and $\vec{B}$. Therefore, a measurement of the electric field can provide information on plasma properties like density and temperature.

One of the main issues not yet solved for the ITER development regards the rise of instabilities which can cause the shut down of the plasma discharge. These conditions generally arise from current density fluctuations (*current driven instabilities*) or from the effect of pressure gradients, combined with the action of the magnetic field curvature (*pressure driven instability*) [21]. Plasma instabilities are linked to the formation of electric fields, which are originated from charge unbalancing, and lead to energy confinement degradation or to the damaging of plasma facing components [4].

Measuring the electric field in a plasma can be a challenging task: probes usually perturb the system, and non-intrusive methods like spectroscopy can not be used for local measurements, as their measure is an average along the line of sight. The EFILE diagnostic (Electric Field Induced Lyman-alpha Emission) is currently under development at PIIM laboratory of Aix-Marseille Université (France), and is a new non-intrusive method for electric field measurements in vacuum or in the edge region of hydrogen plasmas. Using a beam of hydrogen atoms prepared in the metastable $2s$ level, it allows the measurement of electric fields as low as a few V/cm. The principle of this method is the quenching of metastability of the $2s$ state via the Stark mixing effect. Since the beam consists of neutral atoms, it does not affect the electromagnetic configuration, and the radiation detected depends in principle only on the effective electric field inside the measurement region.

1.3 Stark mixing induced transitions

The $2s_{1/2}$ state of the hydrogen atom is metastable, as it has a lifetime of 0.14 s [19], longer than that of other excited levels. This is due to the fact that the transition to the $1s_{1/2}$ level is forbidden in the dipole approximation and the spontaneous transition to the $2p_{1/2}$ level, which has a lower energy, is unlikely because the energy difference is small. The latter transition becomes more likely when the hydrogen atom interacts with an external electric field (eventually oscillating).

The Stark effect describes this interaction, and the transition rate is given by the Lorentzian function (see [18], [27] and appendix B)

$$\gamma_{Stark}(E_0, \omega) = 3 \left(\frac{a_0 e E_0}{\hbar} \right)^2 \frac{\Gamma}{\left(\frac{\Gamma}{2}\right)^2 + (\omega - \omega_{12})^2} \tag{1.1}$$

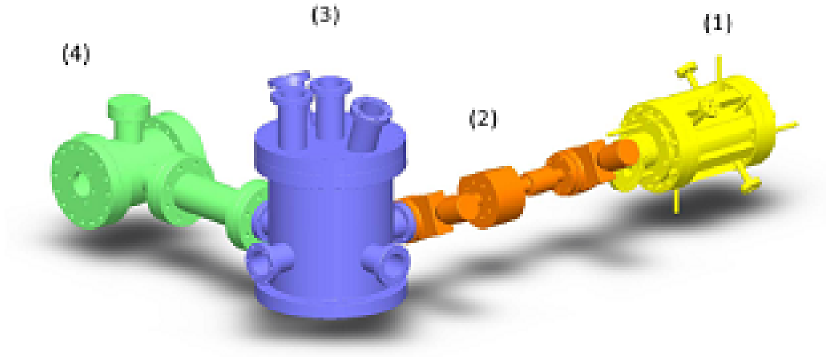

Figure 1.2: Scheme of the EFILE diagnostic: (1) Hydrogen plasma source with ion beam extraction Einzel lens; (2) Cs vapour charge-exchange chamber (3) test chamber; (4) Lyman-α detection chamber. Picture taken from [8].

where $a_0 = 0.53\,\text{Å}$ is the Bohr radius, e is the elementary charge, $\hbar$ is the reduced Plank constant, E_0 and ω are respectively the amplitude and the oscillation angular frequency of the electric field. The curve is peaked at $\omega_{12}/2\pi = (E_{2s} - E_{2p})/h = 1058\,\text{MHz}$, which is the resonance frequency corresponding to the energy difference of the two levels, called Lamb shift [2]. $\Gamma/2\pi = 100\,\text{MHz}$ is the transition rate of the $2p_{1/2}$ state and corresponds to the full width at half maximum of the curve.

After passing in the $2p$ state, the atom decays to the $1s_{1/2}$ level emitting Lyman-α radiation ($2.47 \times 10^{15}\,\text{Hz}$ or $121.6\,\text{nm}$ which is in the UV range), and the intensity of the radiation depends on the number of atoms that are in the $2p$ state. Therefore, assuming the only way to populate this level is the Stark mixing, by measuring the light intensity it is possible to infer the magnitude of the electric field.

1.4 Experimental set-up

The EFILE diagnostic is designed to verify the theoretical behaviour predicted by equation 1.1. Its set-up consists of four different parts, as shown in figure 1.2. In the first part a proton beam is extracted from a hydrogen plasma, and collimated using Einzel lens. The optimal conditions for the plasma production were defined in [18] and are reported in the following sections. The beam is then neutralized and excited to the $2s$ state, exploiting a resonant charge-exchange process between hydrogen and caesium. The metastable beam is then injected into a test chamber, where a known electric field is produced, and finally the induced Lyman-α signal is collected using a

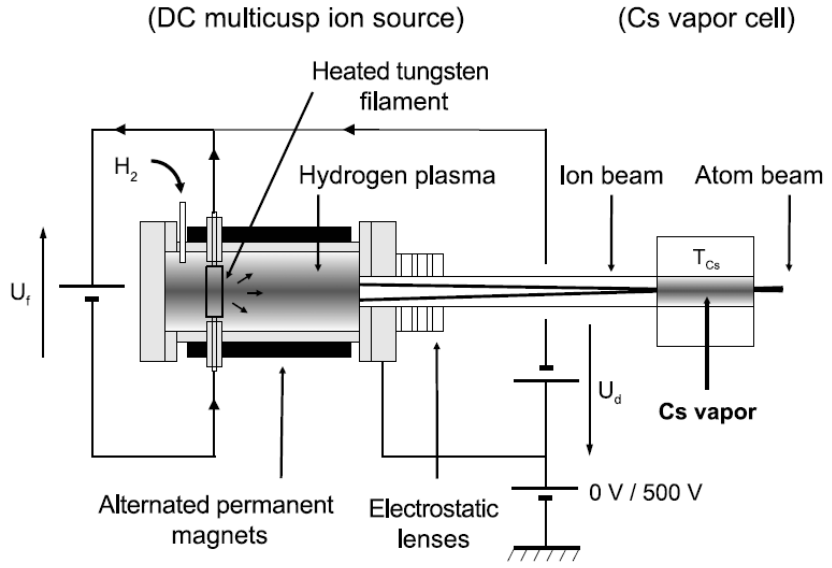

Figure 1.4: Scheme of the ion source, taken from [4].

photomultiplier connected to a lock-in amplifier. When the apparatus is not in use, a background pressure of about 10^{-7} mbar is maintained in the entire system.

1.4.1 The source chamber and the caesium oven

A cylindrical vessel of 166 mm length and 100 mm inner diameter, with the axis parallel to the floor, is filled with molecular hydrogen at a pressure around 10^{-5} mbar. A hydrogen plasma is produced inside using a hot cathode discharge: a voltage $U_f = 10\,\text{V}$ is applied to a tungsten filament, resulting in a 15 A current which heats it. The entire filament is polarised at $U_d = -80\,\text{V}$ with respect to the chamber, accelerating the emitted thermionic electrons and igniting the plasma. The discharge current is between 1 and 1.3 A. To better confine the plasma and to increase the electron density, a set of eight magnets of alternate polarity is placed around the vessel. The source scheme is presented in figure 1.4.

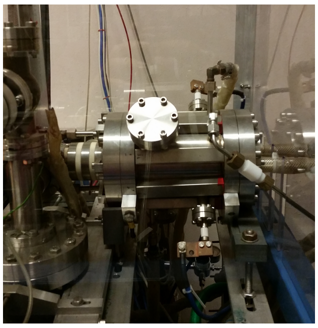

Figure 1.3: The source and the Einzel lens.

The entire source chamber can be polarised at 500 V with respect to the ground, allowing the extraction of a positively charged beam, which

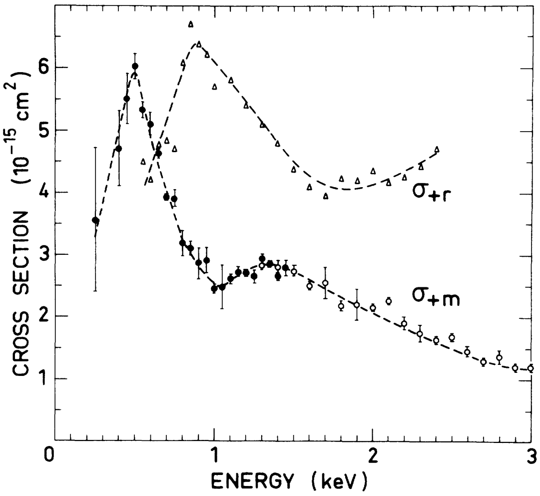

Figure 1.5: Cross section for the production of $H^0(2s)$ (σ_{+m}) and $H^0(2p)$ (σ_{+r}) from reaction 1.2. Picture taken from [24].

is focused by three subsequent circular electrodes (Einzel lens) at different voltages: 200 V, −1300 V and ground from upstream to downstream. The resulting beam is about 2 cm wide and carries a current between 0.1 μA and 1 μA. It mainly consists of three different species: H^+, H_2^+ and H_3^+ [4]. The energy of the beam is peaked at 500 eV, with a dispersion of about 10 eV [18]. This value is far less than the mass of the species (which are of the order of 1 GeV) and therefore relativistic effects can be neglected.

After the extraction, the beam enters in a tube where 5 g of caesium are heated and vaporised by means of a set of resistors. The tube can be completely isolated from the rest of the apparatus by valves, allowing to open the source and test chambers without compromising caesium integrity. The interaction between H^+ and Cs atoms produces neutral hydrogen in the $2s$ and $2p$ levels, following the reaction

$$H^+ + Cs \rightarrow H(2s); H(2p) + Cs^+ + 0.49\,eV \tag{1.2}$$

The collision is almost elastic and, as the caesium mass is larger than that of the proton (the ratio is 132 : 1) the energy of the just neutralised beam can be considered unchanged.

The cross section of reaction 1.2 depends on the beam energy and the production of H($2s$) has a peak at 500 eV (see figure 1.5): this is why the source has been polarised at 500 V; it also depends on the temperature of the caesium oven [27].

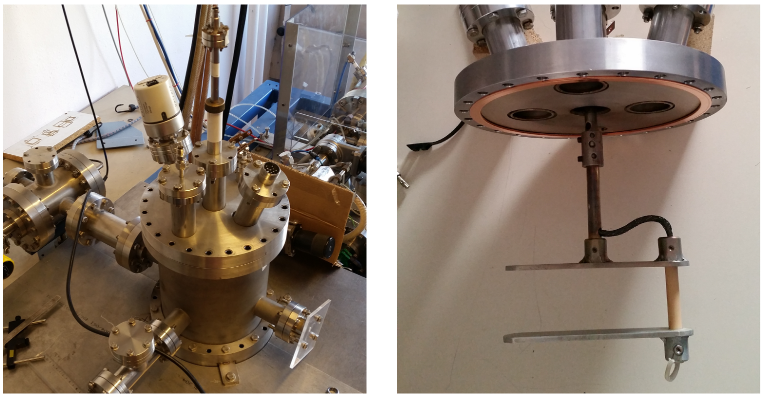

(a) *The test chamber.* (b) *The plates.*

Figure 1.6: The test chamber and the plates.

1.4.2 The test chamber and the acquisition system

After the neutralisation, the beam reaches another cylindrical vessel of length 250 mm and diameter 200 mm, with axis perpendicular to the floor. Here an electric field can be generated by means of two metallic plates, placed at a fixed distance of 50 mm: the lower one can be polarised up to $\pm 600\,\mathrm{V}$ with a static voltage or it can be connected to a radio frequency generator APSIN2010HC which can deliver, combined with an amplifier R&K-AA-200OS, up to 2 W of power. Photos of the test chamber and of the Lyman-α detection chamber and of the plates are shown in figure 1.6. As the distance between the caesium oven and the test chamber is around 30 cm and the energy of the beam is 500 eV, the neutralised particles travel for about $10^{-6}\,\mathrm{s}$ before reaching the plates. Therefore, since the $2p$ lifetime is of the order of $10^{-9}\,\mathrm{s}$, the hydrogen atoms produced in the $2p$ level all decay to the ground state before entering the measurement region.

The Lyman-α signal, which therefore is due to the atoms in the $2s$ state, is detected by a photomultiplier Hamamatsu R1259, placed inside a cylindrical vessel. The PM is isolated from the test chamber by a MgF_2 window, transparent to UV light. The electrical signal produced is sent to a lock-in amplifier AMETEK 5210: this way it is possible to identify the radiation emitted by the atoms from the background by modulating the intensity of the beam with a reference frequency of 1 Hz. Both plate polarisation and lock-in data acquisition can be remotely controlled [12]. The use of the lock-in amplifier implies that the diagnostic can only measure stable state electric fields, because the detected signal is an average over a few beam modulations (an integration time of 3 s was used).

Chapter 2

Mathematical model

In this chapter, a mathematical description of the measurements is presented. The transition rate 1.1 is applied to the EFILE facility, and geometrical issues linked to the experimental set-up are treated.

The EFILE test chamber was originally designed to work with static fields. The plates shown in figure 1.6 (b) act like a capacitor, generating a field mostly localized and constant between them. The idea is that the hydrogen beam in the metastable $2s$ state undergoes the Stark mixing transition only in the region between the plates, allowing a direct measure of the field in that region. However, edge effects are relevant with the set-up used, and will therefore be taken into account.

2.1 Refinement of the transition rate

Expression 1.1 has been obtained by considering only $2s$ and $2p$ fine structure, given by the Lamb shift, and it is valid in a small field approximation[1]. The transition probability can be refined by considering the hyperfine structure of the $n = 2$ energy levels. As reported in appendix A, there are four possible hyperfine states for the $2s_{1/2}$ and $2p_{1/2}$ levels, corresponding to the four possible combinations of quantum numbers F and m_F, associated respectively to the total angular momentum of the atom and to its projection onto a given axis. The selection rules for the allowed transitions between $2s_{1/2}$ and $2p_{1/2}$ are ([6], [20], [23] and [29])

$$\Delta F = 0, \pm 1 \text{ with } F = 0 \rightarrow F = 0 \text{ forbidden } ; \quad \Delta m_F = 0$$

---

[1] $E_0 \ll 26\,000\,\mathrm{V\,m^{-1}}$ for a static field or $E_0 \ll 1800\,\mathrm{V\,m^{-1}}$ for a resonant field. These values were calculated in [27].

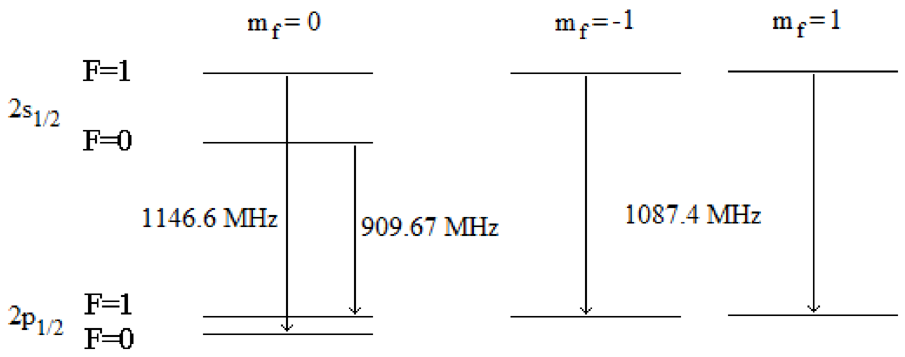

Figure 2.1: Allowed transitions from $2s_{1/2}$ to $2p_{1/2}$ (picture taken from [27] page 6).

Table 2.1: Allowed transitions from $2s_{1/2}$ to $2p_{1/2}$. Energy calculations are reported in appendix A.

$2s_{1/2}$	$2p_{1/2}$	ΔE (eV)	$\nu = \Delta E/h$ (MHz)
$F = 1\,; m_F = 0$	$F = 0\,; m_F = 0$	4.7421×10^{-6}	1146.6
$F = 0\,; m_F = 0$	$F = 1\,; m_F = 0$	3.7621×10^{-6}	909.67
$F = 1\,; m_F = +1$	$F = 1\,; m_F = +1$	4.4971×10^{-6}	1087.4
$F = 1\,; m_F = -1$	$F = 1\,; m_F = -1$	4.4971×10^{-6}	1087.4

and

$$F = 1 \to F = 1 \text{ forbidden if } m_F = 0$$

In figure 2.1 and table 2.1 the four possible transitions are shown. It is to be noted that the last two have the same energy.

Each of the four states before mentioned has its own transition probability, given by equation 1.1

$$\gamma^i_{Stark}(E_0, \omega) = 3\left(\frac{a_0 e E_0}{\hbar}\right)^2 \frac{\Gamma}{\left(\frac{\Gamma}{2}\right)^2 + (\omega - \omega^i_{12})^2}$$

with the index i corresponding to one of the four transitions of frequency $\omega^i_{12} = 2\pi\nu^i$, where the ν^i are the ones reported in table 2.1.

Let n_{2s} be the number of atoms in the $2s$ state. Each of these atoms is in one of the four hyperfine states of the $2s$ level, and it is therefore possible to write $n_{2s} = \sum_{i=0}^{4} n^i_{2s}$, where n^i_{2s} is the number of atoms in the i-th hyperfine state. The variation of n^i_{2s} in time dt, due to an electric field of intensity E_0 and frequency ω, is given by

$$\mathrm{d}n^i_{2s} = -\gamma^i_{Stark}(E_0, \omega) n_{2s} \mathrm{d}t \tag{2.1}$$

and the total variation of n_{2s} is

$$\mathrm{d}n_{2s} = \sum_{i=0}^{4} \mathrm{d}n_{2s}^{i} = \left(\sum_{i=0}^{4} \gamma_{Stark}^{i} n_{2s}^{i} \right) \mathrm{d}t \tag{2.2}$$

As reported in [14], the probability of finding a hydrogen atom in one of the $2s_{1/2}$ hyperfine states is the same. The variation of n_{2s} is therefore

$$\mathrm{d}n_{2s} = -\frac{1}{4} \left(\sum_{i=0}^{4} \gamma_{Stark}^{i} \right) n_{2s}\mathrm{d}t = -\gamma(E_0, \omega) n_{2s}\mathrm{d}t \tag{2.3}$$

where $\gamma(E_0, \omega)$ is the total transition rate for the Stark mixing of the $2s$ and $2p$ levels, given by

$$\gamma(E_0, \omega) = \frac{3}{4}\Gamma \left(\frac{a_0 e}{\hbar} \right)^2 \sum_{i=0}^{4} \frac{E_0^2}{\left(\frac{\Gamma}{2}\right)^2 + (\omega - \omega_{12}^{i})^2} = f(\omega) E_0^2 \tag{2.4}$$

with $f(\omega) = \gamma(E_0, \omega)/E_0^2$. Values of $f(\omega)$ for various frequencies are reported in the table below and a plot is presented in figure 2.2.

$\omega/2\pi$ [MHz]	$f(\omega)$ [m^{2}s^{-1}V^{-2}]
0	0.281
1000	25.6
1146.6	57.9
909.67	36.7
1087.4	76.9

2.2 Estimation of the Lyman-α signal

In this section the relation between the electric field and the emitted radiation induced by the electric field itself will be estimated. Let $n_{2s}(\vec{r})$ be a flux (particle per unit time per unit surface) carried by a beam of hydrogen atoms in the metastable state $2s$, with $\vec{r} = (x, y, z)$. The particles are moving along the z axis with a non relativistic speed v, starting at $z = z_S$. The variation of $n_{2s}(\vec{r})$ due to the Stark mixing along a flux line is given by the exponential decay law

$$\mathrm{d}n_{2s}(\vec{r}) = -\gamma(\vec{r}, \omega) n_{2s}(\vec{r})\mathrm{d}t = -\gamma(\vec{r}, \omega) n_{2s}(\vec{r}) \frac{\mathrm{d}z}{v} \tag{2.5}$$

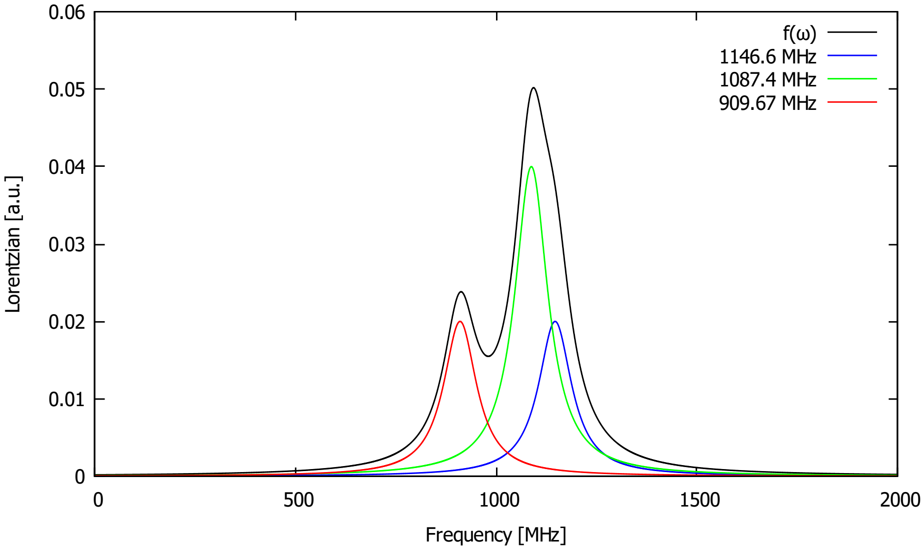

Figure 2.2: Plot of $f(\omega)$ and of the four Lorentzians.

where $\gamma(\vec{r}, \omega)$ is given by 2.4 and can vary along the trajectory due to the varying amplitude of the electric field. The integration gives

$$n_{2s}(\vec{r}) = n_{2s,z_S}(x, y) \exp\left(-\int_{z_S}^{z} \gamma \frac{\mathrm{d}z'}{v}\right) \tag{2.6}$$

where $n_{2s,z_S}(x, y)$ is the flux of particles at $z = z_S$. The flow rate is then obtained by integrating over the beam section Σ

$$N_{2s}(z) = \int_{\Sigma} n_{2s}(\vec{r})\mathrm{d}x\mathrm{d}y = \int_{\Sigma} n_{2s,z_S}(x, y) \exp\left(-\int_{z_S}^{z} \gamma \frac{\mathrm{d}z'}{v}\right)\mathrm{d}x\mathrm{d}y \tag{2.7}$$

Assuming that the photomultiplier can view the region of the beam from z_0 to $z_1 = z_0 + \Delta z$, the intensity I of the radiation emitted by the beam and detected is proportional to the opposite of the variation of $N_{2s}(z)$ in this interval:

$$I = -\beta\Delta N_{2s} = \beta \int_{\Sigma} n_{2s,z_S}(x, y) e^{-\int_{z_S}^{z_0} \gamma \frac{\mathrm{d}z}{v}} \left(1 - e^{-\int_{z_0}^{z_0+\Delta z} \gamma \frac{\mathrm{d}z}{v}}\right) \mathrm{d}x\mathrm{d}y \tag{2.8}$$

and the proportionality coefficient β is related to the photomultiplier properties (mainly efficiency and solid angle). This equation holds for a completely general electric field configuration, and shows that a measure in the $z_0 < z < z_1$ region is not independent from the field at $z < z_0$.

Assuming the coefficient β and the density distribution $n_{2s}(x, y, z_S)$ are known, a relation between the electric field in the measurement region and

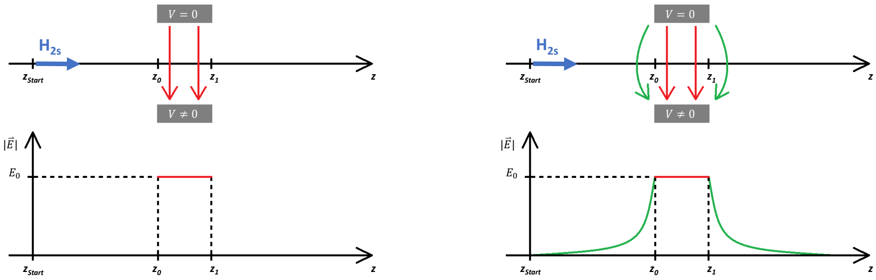

(a) *Confined and static electric field.* (b) *Inclusion of edge effects.*

Figure 2.3: Electric field configurations.

the Lyman-α signal can be established only if the region before is field-free, or, which is the same, if the spatial field distribution is known.

Equation 2.8 will now be used to describe the emission due to the beam passing between two metallic plates of width Δz, one of which is polarised with a static voltage ($\omega = 0$), while the other is grounded. The plates act therefore as a capacitor, and an electric field between them is generated.

Confined and static electric field

Let the electric field be perfectly confined in the region between the plates, as in a perfect capacitor, and let E_0 be its absolute value. A graphic representation is shown in figure 2.3 (a).

If the beam density is constant along the x and y directions and Δz is supposed to be small compared to the typical variation size of the electric field, equation 2.8 can be simplified as

$$I \approx \beta N_{2s}(0)\left(1 - e^{-f(0)\frac{\Delta z}{v}E_0^2}\right) \approx \beta N_{2s}(0) f(0) \frac{\Delta z}{v} E_0^2 \tag{2.9}$$

where $f(0)E_0^2 = \gamma(E_0, 0)$ from 2.4, and the last equality holds for $E_0 \ll \sqrt{v/(\Delta z f(0))}$. There is therefore a one to one relation between the electric field and the detected radiation, allowing a direct measure of the electric field in the Δz region.

This configuration is represented by an ideal capacitor, without edge effects. For a static polarisation, the plates inside the test chamber act like this for small values of the voltage applied to the lower plate. As the voltage increases, the intensity of the edge field increases as well, and the hydrogen beam experiences an intense electric field before entering in the measurement

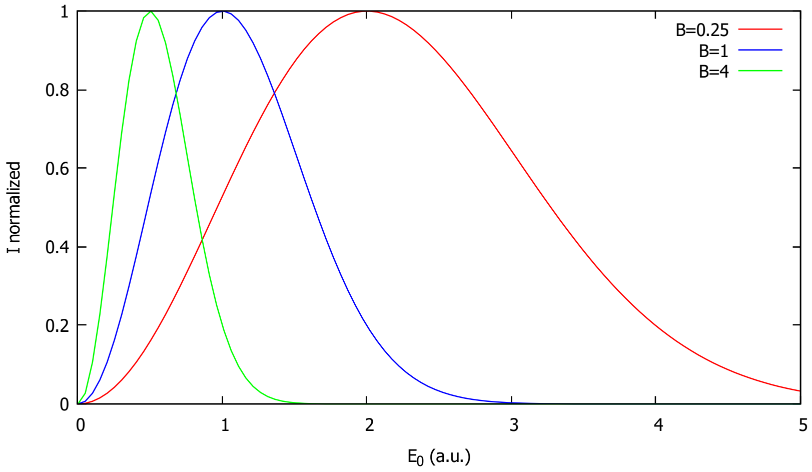

Figure 2.4: Theoretical model of the Lyman-α signal for a static field.

region. Therefore to have an estimation of the Lyman-α signal it is necessary to consider the variation due to $\int_{z_S}^{z_0} f(\omega) E_0^2 \frac{\mathrm{d}z}{v}$.

Inclusion of edge effects

Let the intensity of the electric field before z_0 behave as

$$E(z < z_0) = E_0 \left(\frac{z - z_S}{z_0 - z_S} \right)^{\delta} \tag{2.10}$$

where E_0 is the value at $z = z_0$ and $\delta > 0$ (a representation is given in figure 2.3 (b)). Upon setting $z_S = 0$, the integration gives:

$$\int_0^{z_0} f(0) E^2(z) \frac{\mathrm{d}z}{v} = \frac{f(0)}{v} E_0^2 \frac{z_0}{2\delta + 1}$$

and the intensity of the signal at a fixed frequency becomes:

$$I \approx \beta N_{2s}(0) e^{-\frac{f(0)}{v} \frac{z_0}{2\delta+1} E_0^2} \frac{f(0)}{v} \Delta z E_0^2 = A e^{-B E_0^2} E_0^2 \tag{2.11}$$

where $A = \beta N_{2s}(0) \frac{f(0)}{v} \Delta z$ and $B = \frac{f(0)}{v} \frac{z_0}{2\delta+1}$ and the same assumptions as before are used.

Like in the confined case, the new function behaves as $I \approx A E_0^2$ for small values of E_0, but it also tends to zero for $E_0 \to +\infty$, and it has a maximum at $E_0 = \sqrt{1/B}$ of value $I_{max} = \frac{A}{B} e^{-1}$. It is therefore not possible to invert the function and to infer the intensity of the electric field from the signal, as this is not a bijection.

To remove the dependence on parameter A, and therefore on beam and detector properties, it is useful to normalize I with respect to I_{max}:

$$I_{norm} = Be^{1-BE_0^2}E_0^2 \tag{2.12}$$

In figure 2.4 a plot of I_{norm} for different values of B is presented.

For a static field ($f(0) = 0.281\,\mathrm{s}^{-1}\,\mathrm{m}^2\,\mathrm{V}^{-2}$), assuming $\delta = 2$, $z_0 = 0.1\,\mathrm{m}$ and protons of $500\,\mathrm{eV}$ ($v = 3.09 \times 10^5\,\mathrm{m/s}$) the maximum is reached at $E_{0,max} = 7.4 \times 10^3\,\mathrm{V/m}$, and the voltage difference needed by a capacitor with distance between the plates of $5\,\mathrm{cm}$ to generate this field is $V_{max} = 3.7 \times 10^2\,\mathrm{V}$. This value will be later compared to the experimental results.

Chapter 3

Simulations

To test and calibrate the EFILE diagnostic, an accurate estimation of the electric field encountered by the beam inside the test chamber is needed. This is done by solving Maxwell's equations with the appropriate boundary conditions. As the geometry of the chamber is not simple, it is necessary to numerically solve the equations. For these calculations, the software CST Studio Suite [7] was used: Maxwell's equations were solved using a finite element method on a 3D model of the test chamber properly after proper meshing of the volume. A cartesian reference system is used: the beam moves along the z axis, the vertical direction is the y axis and the x indicates the horizontal direction perpendicular to the beam. The center of the plates is located at point $P = (0, -45\,\mathrm{mm}, 0)$.

3.1 Model of the test chamber

A CAD model of the test chamber was developed to reproduce the correct geometry of all the elements inside: the vessel, the plates and a probe used for electric field measurements. All the elements are shown in figure 3.1.

The vessel is made of steel and consists of a cylinder of 250 mm inner height and a diameter of 200 mm. Four cylinders of 35 mm inner diameter are placed on the side face. Their axes are perpendicular to each other and lie on a plane orthogonal to the main cylinder axis, at 80 mm from the bottom of the cylinder. The beam enters the chamber through one of them, and the photomultiplier line of sight passes through a perpendicular one. Five more cylinders of different diameters are placed on the upper face of the vessel. Through the one placed at the center, the polarised plates are inserted inside the chamber, while the others are used for measuring the inner pressure or to inject argon gas. In the lower part there is another cylinder of 225 mm inner

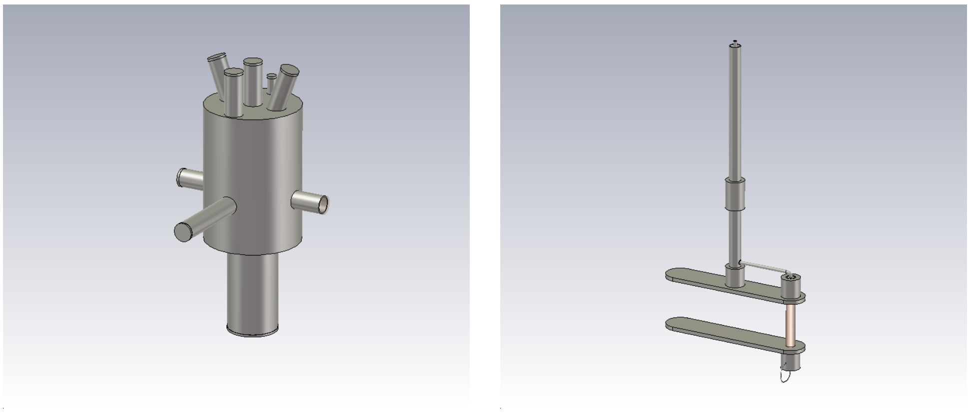

(a) *The vessel.*

(b) *The plates.*

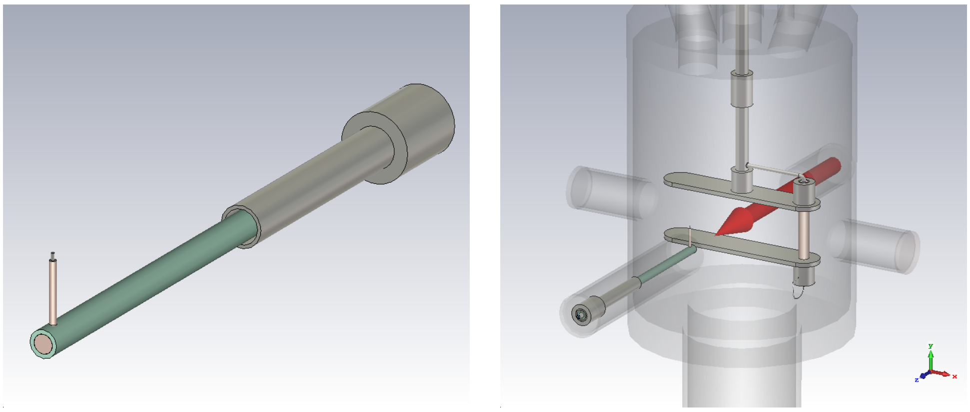

(c) *The probe.*

(d) *The interior of the vessel. The red arrow represents the $H^0(2s)$ beam.*

Figure 3.1: CAD model of the test chamber.

length and 100 mm of diameter; it connects the chamber to the pumping system. The interior of the vessel is considered vacuum.

The system used to generate the electric field inside the test chamber consists of two metallic plates of 160 mm length along the x axis, 30 mm width along the z axis and 4 mm thickness along the y axis, through which the $H^0(2s)$ beam passes. The distance between them is 50 mm, and they are supported by an alumina cylinder, of 12 mm diameter. The plates are fixed to a steel tube, which is used to set their position with respect to the beam. A coaxial cable RG58 passes through this tube and the alumina cylinder, allowing a polarisation of the lower plate with respect to the other, which is grounded. The upper termination of the coaxial cable can be connected to an external generator, and for the simulation a signal entry port is defined there.

To have a rough estimation of the electric field inside the vessel, a probe was built from a coaxial cable, whose end has been bared and bent in the orthogonal direction. The probe is placed on the same axis as the beam.

3.2 Static field

The first simulated configuration was a static field. The equation solved is the Poisson equation [15]:

$$\nabla \cdot (\epsilon_r \nabla \Phi) = \rho / \epsilon_0 \tag{3.1}$$

where Φ is the electrostatic potential, ρ is the charge density, ϵ_0 is the vacuum permittivity ($8.85 \times 10^{-12}\,\mathrm{F\,m^{-1}}$) and ϵ_r is the relative permittivity of the various materials simulated. As in the experimental case, the electrostatic voltage of the coaxial cable used for the polarisation of the lower plate was set to a fixed value $\Phi = V_0$, while the voltage of the vessel walls was set to zero (Dirichlet condition); furthermore the charge density ρ was set to zero, because it is assumed that there were no free charges. The results of the simulation for $V_0 = 50\,\mathrm{V}$ are shown in figure 3.2 and 3.3. As can be seen from the plots, the field is almost constant on the horizontal plane between the plates ($x - z$ plane), but varies in the vertical direction (y axis): this is due to the fact that the distance between the plates (50 mm) is larger than their width (30 mm). Moreover, the behaviour along the z axis is comparable with the one described in section 2.2, and therefore equation 2.11 can be used for fitting experimental data.

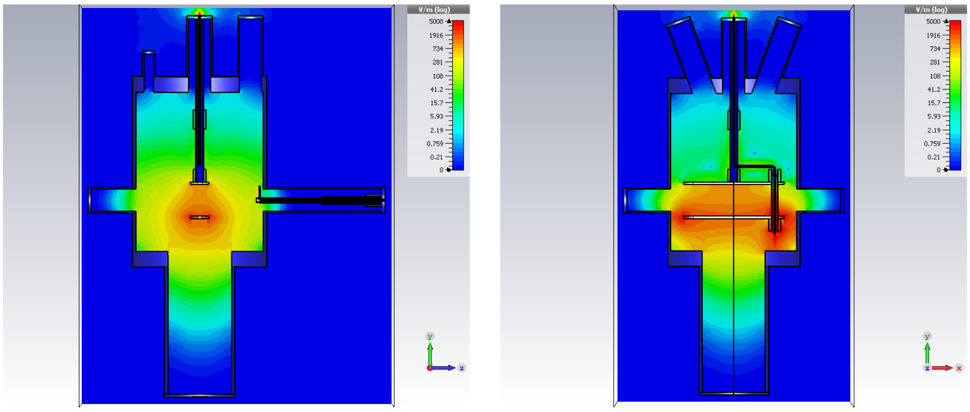

(a) *Field amplitude on the $y-z$ plane.* (b) *Field amplitude on the $x-y$ plane.*

Figure 3.2: Field maps for the simulation with $V_0 = 50\,\mathrm{V}$.

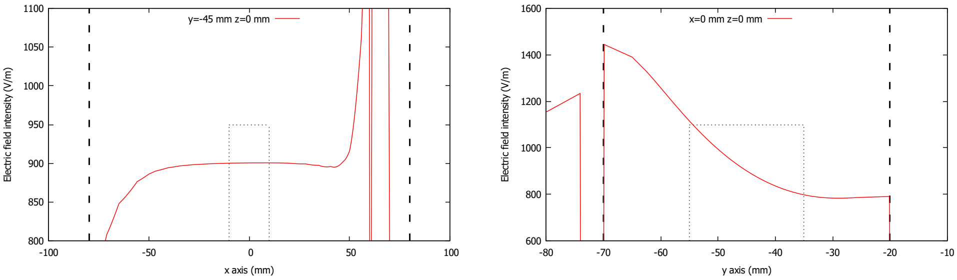

(a) *Field amplitude along the x axis.* (b) *Field amplitude along the y axis.*

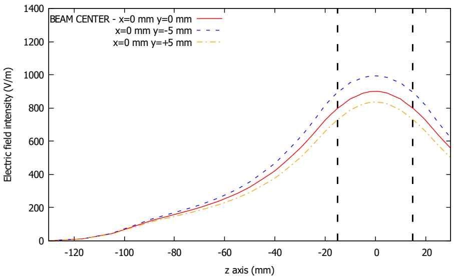

(c) *Field amplitude along the z axis.*

Figure 3.3: Plot of field amplitude along the axis. The black vertical dashed lines in each graph show the dimension of the plates. For the x and y axis plots, the estimated beam profile is also presented (with arbitrary height), to show the variation of the field along the beam dimension.

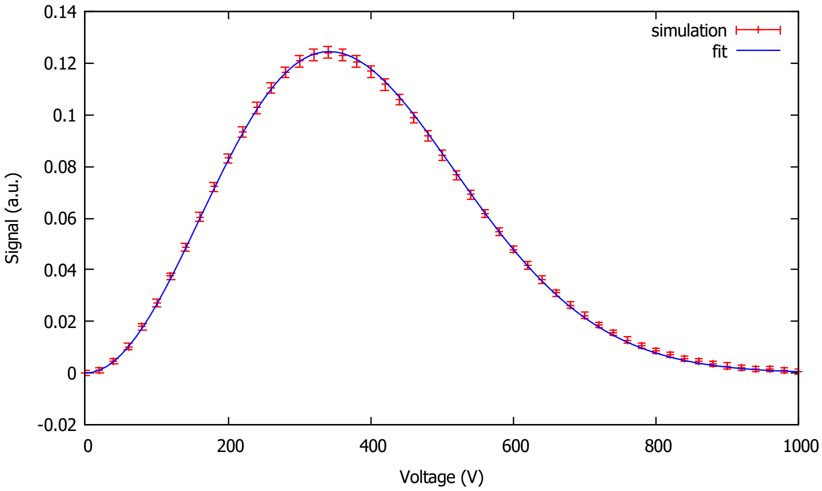

Figure 3.4: Numerical simulation of the Lyman-α signal for a static field and fit.

3.2.1 Simulation of the Lyman-α signal

The simulated electric field was then used to estimate the expected Lyman-α signal for different voltages applied to the lower plate. As Maxwell's equations are linear, changing the value of V_0 does not modify the shape of the simulated electric field: it just linearly modifies its magnitude. Given the electric field for a defined V_0, $\vec{E}_{V_0}$, the electric field for $V_0' = \alpha V_0$ is given by

$$\vec{E}_{\alpha V_0} = \alpha \vec{E}_{V_0}$$

and therefore it was not necessary to repeat the simulation for different values of V_0.

Numerical calculations of equation 2.8 for different values of V_0 were performed with a code written in the IDL language, upon setting $\beta = 1$, defining the detection region by the photomultiplier characteristics (his active surface is a rectangle of 12 mm length in beam direction and 8 mm height), assuming the beam density to be constant in the x and y directions and the beam section to be a circle of 20 mm diameter. The results are shown in figure 3.4, assuming every point is affected by a 1% error.

The picture also shows the best fit of equation $I = A'e^{-B'V_0^2}V_0^2$, which is a modification of equation 2.11, assuming the relation $E_0 = V_0/d$ for a perfect capacitor (d is the distance between the plates) and with the obvious correspondences

$$A' = A/d^2 \quad ; \quad B' = B/d^2$$

The fitting curve follows quite well the simulated data, and the results are

$$A' = (2.894 \pm 0.010) \cdot 10^{-6}\, V^{-2}$$
$$B' = (8.550 \pm 0.017) \cdot 10^{-6}\, V^{-2}$$

which predicts a maximum of the signal at $V_{max} = 1/\sqrt{B'} = (342.0 \pm 0.2)\, V$, not far from the 370 V calculated in section 2.2. The ratio $(z_0 - z_S)/(2\delta + 1)$ can be derived too (the notation is the same used in the previous chapter and $z_0 - z_S$ stands for the length travelled by the beam where the electric field is non zero before passing between the plates):

$$\frac{z_0 - z_S}{2\delta + 1} = B' d^2 \frac{v}{f(0)} = (2.350 \pm 0.005)\,\mathrm{cm} \tag{3.2}$$

where $f(0) = 0.281\,\mathrm{s}^{-1}\,\mathrm{m}^2\,\mathrm{V}^{-2}$, $v = 3.09 \times 10^5\,\mathrm{m/s}$, $d = 5\,\mathrm{cm}$ and only B' is assumed to have an error. Assuming the length $z_0 - z_S$ to be comparable to the radius of the vessel (10 cm), it gives $\delta \approx 1.6$.

3.3 Radio frequency field

The transition rate 2.4 depends on the frequency of the field, and resonates around 1 GHz, in the radio frequency (RF) domain. The ideal case is that the model derived in section 2.2 for a static electric field mostly confined between the plates can also be used to describe a radio frequency perturbation. Equation 2.9 shows that if the magnitude of the field is the same for every frequency, the signal should behave as the $f(\omega)$ function of figure 2.2.

To test the radio frequency behaviour, the lower plate was polarised with an oscillating voltage (as done in [28] and [13]), with frequencies up to 2 GHz, and spectra of the Lyman-α signal were acquired for a fixed power emitted by the generator. An example is presented in picture 3.5. Instead of showing the expected behaviour, the spectrum presents well defined peaks of different height and width of only few MHz, which could be reproduced in repeated measurements at different times, but would change if the positions of the objects inside the vessel were modified.

This is due to the fact that the dimensions of the test chamber is comparable with the wavelength of the oscillating electric field (around 30 cm for a 1 GHz electromagnetic wave), and the vessel, which is made of metal, acts as a resonant cavity [10]. The field shape and its intensity depend on frequency, geometrical design and material details of the chamber, and on the transmission line characteristics. The CST Microwave Studio tool of CST Studio Suite was used to verify and investigate the effect on RF voltages of the experimental set-up.

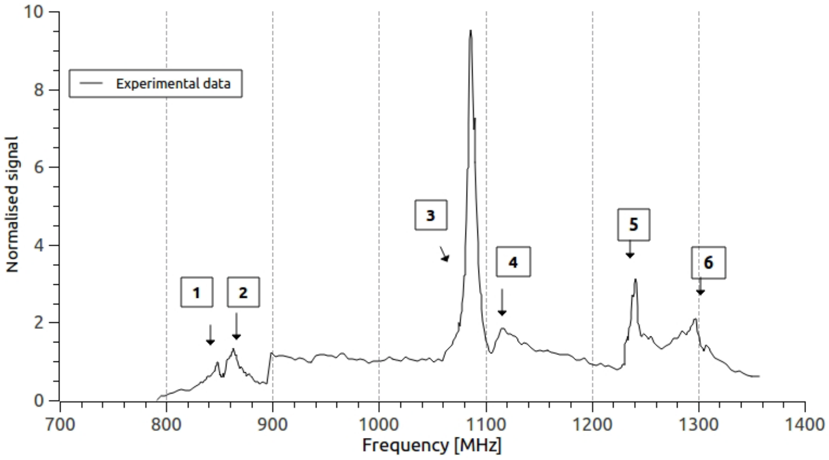

Figure 3.5: Example of Lyman-α spectrum, showing 6 different peaks. Picture taken from [28], page 16.

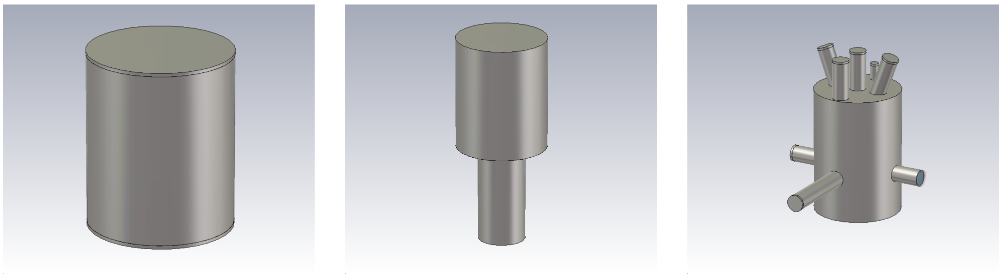

(a) *Simple cylinder.* (b) *With low cylinder.* (c) *With small cylinders.*

Figure 3.6: Different vessels simulated.

3.3.1 Eigenvalues

Firstly, an evaluation of the resonant frequencies of the cavity was performed. The equation solved is [15]:

$$\nabla \times \left[\mu_r^{-1} \nabla \times \vec{E}(\vec{x})\right] = \epsilon_r \frac{\omega^2}{c^2} \vec{E}(\vec{x}) \tag{3.3}$$

where μ_r is the magnetic relative permeability, ϵ_r is the electric relative permittivity, c is the speed of light and ω is the resonant frequency. All the metal objects were considered as perfect electric conductors (PEC), and tests with different configurations were performed.

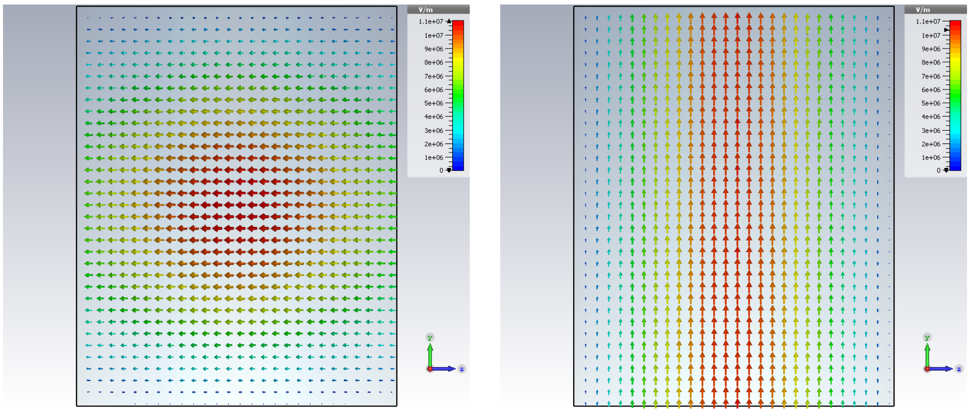
(a) *TE mode.* (b) *TM mode.*

Figure 3.7: Example of TE and TM mode in a cylinder. The amplitude of the field is such that the entire energy stored in the electromagnetic field inside the vessel is 1 J.

Empty vessel

The easiest approximation is to consider the vessel as a cylinder. In this configuration the resonant frequencies have two analytical expressions, given by [30]

$$\nu_{nml}^{TE} = \frac{c}{2\pi}\sqrt{\left(\frac{p'_{nm}}{D/2}\right)^2 + \left(\frac{l\pi}{L}\right)^2} \tag{3.4}$$

and

$$\nu_{nml}^{TM} = \frac{c}{2\pi}\sqrt{\left(\frac{p_{nm}}{D/2}\right)^2 + \left(\frac{l\pi}{L}\right)^2} \tag{3.5}$$

where c is the speed of light, D and L are the diameter and the height of the cylinder respectively, n, m and l are natural numbers, p_{nm} is the mth zero of the nth order Bessel function and p'_{nm} is the mth zero of the derivative of the nth order Bessel function. Equation 3.4 describes resonant modes with the electric field perpendicular to the cylinder axis (*Transverse Electric* or TE modes, see figure 3.7 (a)), while equation 3.5 describes resonant modes with the magnetic field perpendicular to the cylinder axis (*Transverse Magnetic* or TM modes, see figure 3.7 (b)). The resonant frequencies below 2 GHz are shown in table 3.1 and in figure 3.8 (a), compared with the results of CST calculations. It can be noted that simulations and analytical results are in good agreement, except for three modes: TE_{110}, TE_{210} and TE_{010}. This is due to the fact that these modes have non zero tangential electric field on the walls of the cylinder, and therefore are not allowed for a cylinder with

Table 3.1: Comparison between analytical and numerical calculations of the eigenfrequencies for the simple cylinder.

Mode	ν^{Th} (GHz)	ν^{Sim} (GHz)	$\nu^{Sim} - \nu^{Th}$ (GHz)
TE_{110}	0.878 492 3	NOT PRESENT	
TE_{111}	1.063 603	1.063 608	5×10^{-6}
TM_{010}	1.147 425	1.147 430	5×10^{-6}
TM_{011}	1.294 638	1.294 642	4×10^{-6}
TE_{210}	1.457 282	NOT PRESENT	
TE_{112}	1.486 525	1.486 552	27×10^{-6}
TE_{211}	1.575 809	1.575 832	23×10^{-6}
TM_{012}	1.659 697	1.659 731	34×10^{-6}
TE_{010}	1.828 239	NOT PRESENT	
TM_{110}	1.828 239	1.828 285	46×10^{-6}
TE_{212}	1.887 241	1.887 328	87×10^{-6}
TE_{011}	1.924 048	1.924 103	55×10^{-6}
TM_{111}	1.924 048	1.924 117	69×10^{-6}

metallic walls (however the TE_{010} mode has the same eigenfrequency as the TM_{110} mode).

Next, the configuration (b) and (c) of figure 3.6 were simulated, to quantify the contribution of the other elements of the test chamber to the distribution of the resonant frequencies. Results are shown in figure 3.8 (b) and (c). As can be seen, the configuration with a cylinder added below clearly modifies the eigen frequencies, while for the last configuration the differences are small. This is due to the small diameter of the additional cylinders placed on the main cavity, as can be seen from equations 3.4 and 3.5[1]. It is worth noting that the presence of these cylinders breaks the symmetry of the vessel, increasing the number of modes by separating two modes which are degenerate in a cylindrical configuration.

Adding plates and probe

The same calculations were performed for the complete vessel with plates and probe inside. The $0.8 - 1.6$ GHz range was studied, to investigate the behaviour of the system for frequencies near the peaks of the transition probability. Results are presented in figure 3.9. While adding the probe does not

---

[1] For the considered cylinder, the smallest mode is at about 1 GHz. As the smaller cylinders have an inner diameter of 3.5 cm, their lowest resonant frequency is $1\,\text{GHz} \times \frac{20\,\text{cm}}{3.5\,\text{cm}} \approx 6\,\text{GHz}$

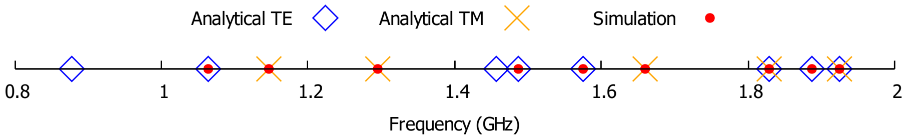

(a) *Comparison between the simulation and the analytical calculation for the simple cylinder of figure 3.6 (a).*

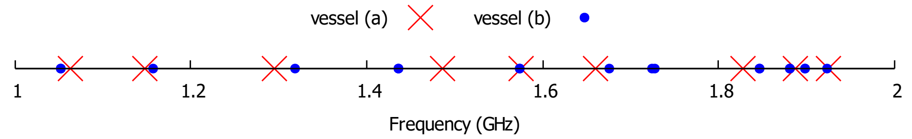

(b) *Comparison between the simulations for the simple cylinder of figure 3.6 (a) and the vessel of figure 3.6 (b).*

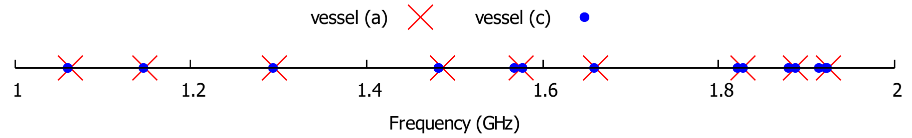

(c) *Comparison between the simulations for the simple cylinder of figure 3.6 (a) and the vessel of figure 3.6 (c).*

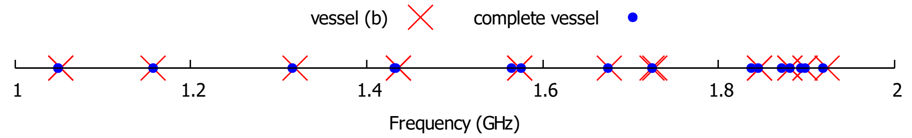

(d) *Comparison between the simulations for the vessel of figure 3.6 (b) and the complete vessel shown in 3.1 (a).*

Figure 3.8: Resonant frequencies of the empty vessel.

Table 3.2: Resonant frequencies of the complete system.

Frequency (GHz)
1.006
1.026
1.102
1.174
1.252
1.399
1.404
1.413
1.497
1.545
1.550

considerably change the resonant frequencies, adding just one resonant mode around 1.1 GHz, the presence of the plates completely changes the distribution, and therefore it is no more possible to recognize standard TM or TE modes. The calculated values are presented in table 3.2. In figure 3.10 some projections of the amplitude of the electric field onto the plane perpendicular to the beam are presented. These pictures show that the shape of the field depends on the excited eigenmode.

3.3.2 The S-parameters

The device was tested with a radiofrequency signal injected through the coaxial cable connected to the lower plate. To study the behaviour of this configuration, calculations simulating the presence of a time varying voltage applied to the entry port were performed. The equations to be solved are equivalent to 3.3 with a source term. The first step was to simulate the *S-parameters* of the system [22] in the frequency range considered ($0.8 - 1.6$ GHz). Assume a n port network and an electromagnetic wave injected through the i-th port. On the j-th port there will be an electromagnetic wave exiting. This configuration can be represented by

$$a_i = \frac{V_i^+}{\sqrt{Z_{c,i}}} = I_i^+ \sqrt{Z_{c,i}} \tag{3.6}$$

$$b_j = \frac{V_j^-}{\sqrt{Z_{c,j}}} = I_j^- \sqrt{Z_{c,j}} \tag{3.7}$$

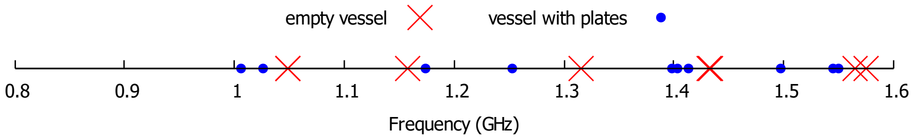

(a) *Comparison between the resonant frequencies of the empty vessel and of the vessel with the plates.*

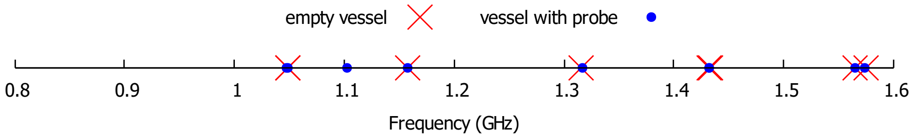

(b) *Comparison between the resonant frequencies of the empty vessel and of the vessel with the probe.*

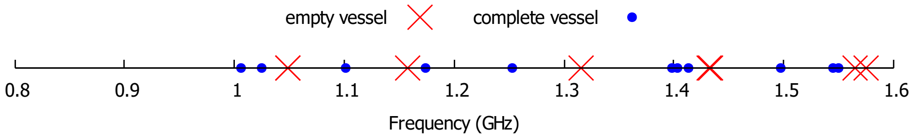

(c) *Comparison between the resonant frequencies of the empty vessel and of the vessel with the plates and the probe.*

Figure 3.9: Resonant frequencies.

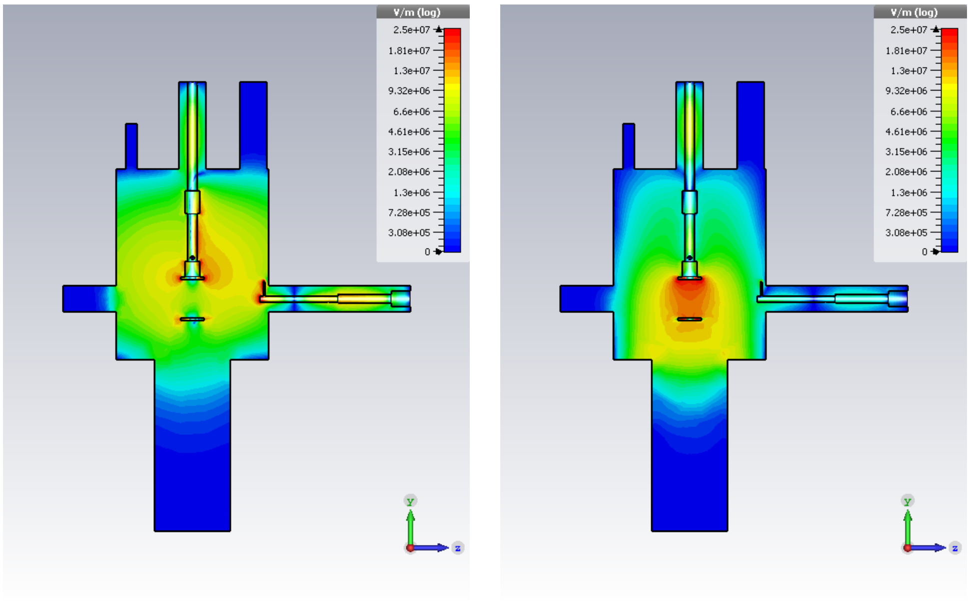

(a) 1.026 GHz (b) 1.252 GHz

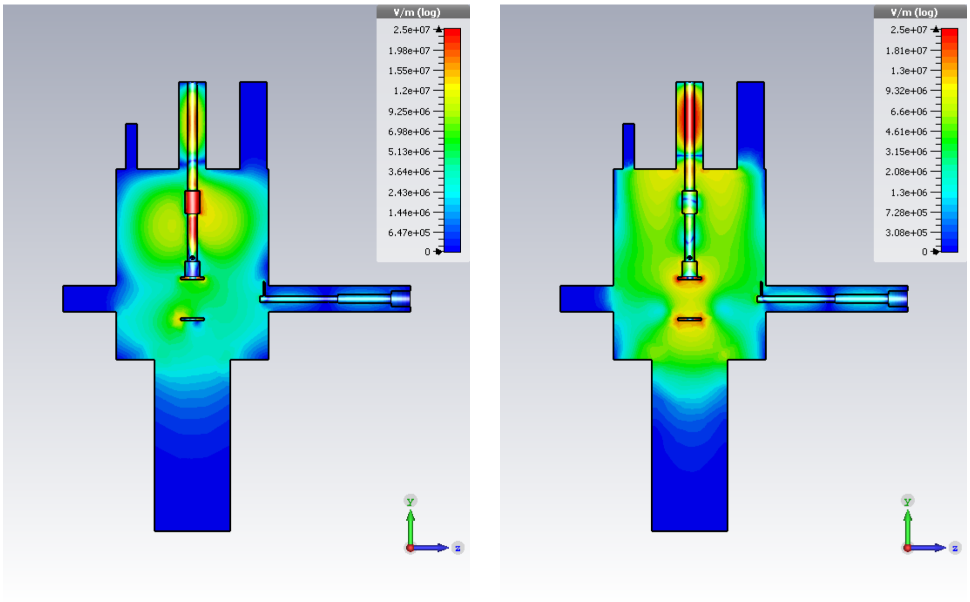

(c) 1.404 GHz (d) 1.550 GHz

Figure 3.10: Projections of the amplitude (in logarithmic scale) of the electric field on the plane perpendicular to the beam for various eigenvalues. The amplitude of the field is such that the entire energy stored in the electromagnetic field inside the vessel is 1 J.

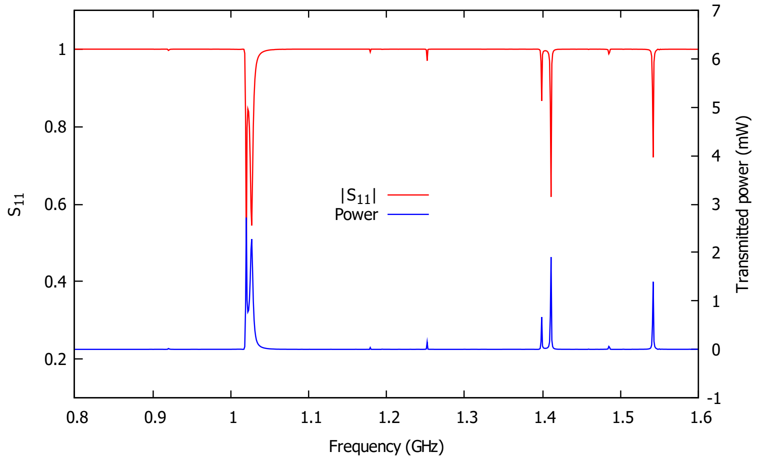

Figure 3.11: S_{11} and simulated transmitted power, with $P_0 = 5\,\mathrm{mW}$.

where V_i^+ and I_i^+ are the voltage and the current at the i-th port carried by the incoming wave, V_j^- and I_j^- are associated to the wave exiting from the j-th port; $Z_{c,k}$ is the impedance of the line connected to the k-th port. The S-parameters is defined as the $n \times n$ matrix with elements

$$S_{ji} = \frac{b_j}{a_i} \tag{3.8}$$

and it describes the response of the system to an electric stimulation of given frequency and power $P_0 = \frac{1}{2}|a_i|^2$.

The EFILE set-up can be seen as one port connected to a cavity. A generator is connected to the port and an electric field is produced inside the vessel. The shape of the field depends on the excited eigenmode, while its amplitude is linked to the power transmitted by the generator. This quantity can be obtained from the S_{11} term of the S-matrix

$$P_T = \frac{1}{2}(|a_1|^2 - |b_1|^2) = \frac{1}{2}|a_i|^2(1 - |S_{11}|^2) \tag{3.9}$$

and it is therefore a measure of the adaptation of the system in response to a stimulation of given frequency. The simulated S_{11} parameter and the corresponding injected power are reported in figure 3.11. The picture shows few sharp well defined peaks of a few MHz width, at the frequency of some of the eigenvalues reported in table 3.2 (1.006 GHz, 1.026 GHz, 1.399 GHz, 1.413 GHz and 1.545 GHz), and other small peaks (1.252 GHz). This explains the behaviour of the spectrum of figure 3.5: the peaks are not linked to the hyperfine structure of the hydrogen atom, but depend on which electromagnetic eigenmodes are excited inside the cavity by the polarised plates. The

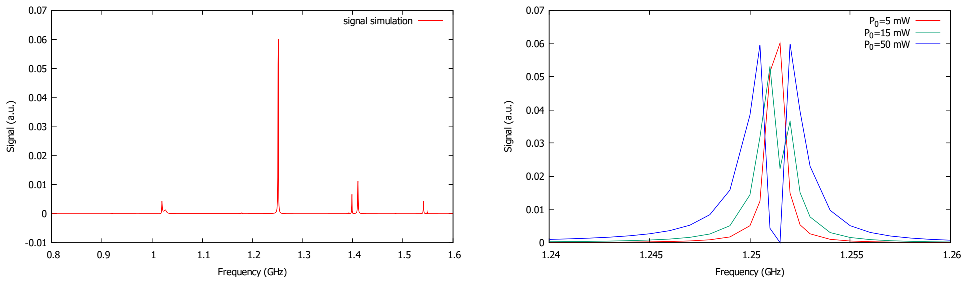

(a) *Entire spectrum for a sinusoidal injected signal of* 5 mW.

(b) *The saturation of the Lyman-α peak at* 1.252 GHz.

Figure 3.12: Lyman-α spectrum simulation.

vessel acts therefore as a selective filter. However, this is just a qualitative explanation: position and amplitude of the real peaks are hard to reproduce, as they strongly depend on the geometry (as shown in the previous section) and also on the power losses, which are not taken into account in these simulations because all metals are approximated as PEC.

3.3.3 Frequency spectrum

The frequency results were used to simulate the Lyman-α frequency spectrum: the electric field generated inside the vessel was recorded and used to evaluate equation 2.8, with the same assumptions as for the static case ($\beta = 1$, the beam is approximated as a homogeneous cylinder of 20 mm diameter and the detection region is a 12 mm × 8 mm rectangle between the plates). Every point in the curve reported in figure 3.12 (a) corresponds to a sinusoidal injected signal of power $P_0 = 5\,\mathrm{mW}$.

As for the static case, saturation can be observed in the frequency spectrum too. Its evidence is the presence of an indentation of the top of the peaks, as shown for instance in figure 3.12 (b), where the Lyman-α peak at 1.252 GHz is calculated for different injected powers simulations. It is to be noted that all the peaks in the Lyman-α spectrum correspond to those of the S_{11} graph but the highest one is at 1.252 GHz, which is not the most adapted frequency. This is due to the shape of the corresponding eigenfrequency: as shown in figure 3.10, at this frequency the electric field is mostly concentrated between the plates, and therefore the field there is more intense, although at other frequencies the transmitted power is higher. This is made clear by looking at figure 3.13, which shows how the electric field varies with frequency along the beam axis.

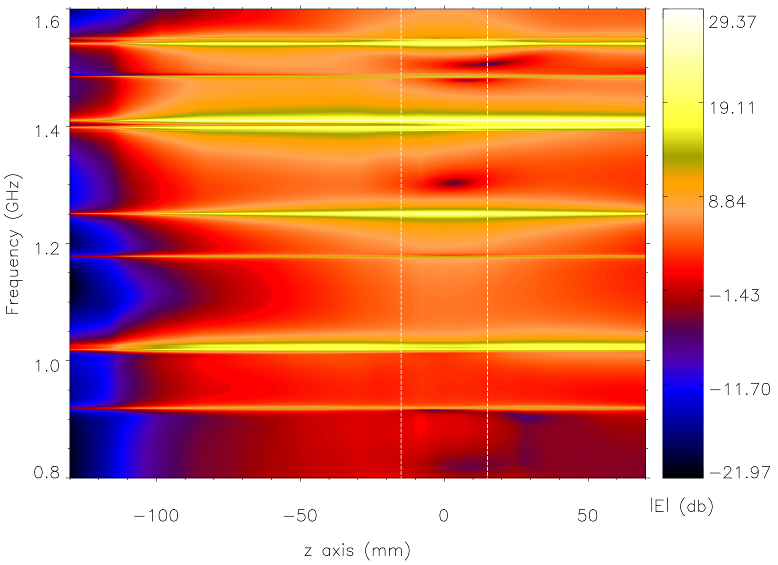

(a) *Variation of the electric field intensity along the beam for the entire frequency range.*

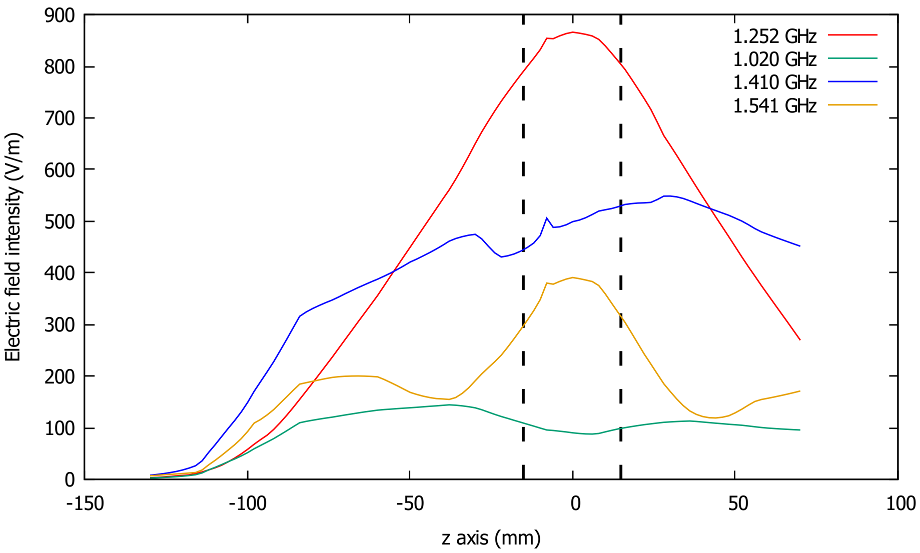

(b) *Plot of selected frequencies.*

Figure 3.13: Behaviour of the electric field's magnitude along the beam line (z axis). The dashed lines identify the borders of the plates.

Chapter 4

Experimental data

In this chapter the acquired experimental data will be presented. As discussed in chapter 2, the behaviour of the Lyman-α signal not only depends on the field in the measurement region, but it is also strictly related to the field in the region previously travelled by the beam. Therefore, as it is not possible to affirm that one measurement correspond to one precise field value (or to an averaged value in the detection region), the best result is to find a correspondence between the measured data and an expected field map.

The signal emitted by the hydrogen beam and detected with the photomultiplier has been processed using a lock-in amplifier AMETEK 5210. All the measurements reported herein were made by pulsing the beam, at a reference frequency of 1 Hz, and recording the results in a computer. The lock-in integration time used was 3 s. This technique allows to discriminate between the noise and the electric signal due to UV light emitted by the beam. The lock-in output can be divided into two parts: the induced emission, due to the electric field present in the test chamber, and the spontaneous emission, due to photons emitted by collisions or by natural lifetime decay, which determines the background. In the following the two contributions are assumed to be independent. The lock-in output is a voltage, and it is proportional to the number of photons per unit time I_{TOT} emitted in the measurement volume, following the relation

$$I_{TOT} = \alpha S \tag{4.1}$$

where S is the output voltage and $\alpha = 4.45 \times 10^7\,\mathrm{s}^{-1}\mathrm{V}^{-1}$ [18] takes into account all the characteristics of the detection apparatus.

For every measure, the the lock-in signal oscillated around a mean value. The σ of these oscillations was interpreted as the σ of the measurements and was observed to be $5\,\mu$V for a signal of $100\,\mu$V, and $10\,\mu$V for a signal of 1000 μV. A linear interpolation has been performed for the intermediate values.

All the measurements reported herein were effectuated with a hydrogen pressure of the order of 10^{-5} mbar inside the source chamber, where a plasma was generated by heating the tungsten filament with a current of about 15 A and accelerating the emitted electrons with a voltage drop of 80 V with respect to the source vessel; the hydrogen ions were extracted by the Einzel lenses, set at a voltage of 1.3 kV with respect to the ground, and accelerated by a 500 V voltage drop; the temperature of the caesium was the same for all the measurements; the pressure inside the test chamber was of the order of 10^{-6} mbar.

The hardest parameter to control is the source chamber pressure, because it depends on the hydrogen temperature which is linked to the heating of the filament. This implies that the ion current extracted from the source is hard to reproduce from one measurement session to another. Therefore, measurements made on different days can present different amplitudes and offsets, although the starting parameters are the same.

4.1 Static field

The first measure was performed with a static voltage applied to the lower plate. To test the goodness of the model for experimental data, the validity limits of the theoretical prediction have to be considered. As reported in section 2.1, the transition rate of equation 1.1 is a good approximation if $E_{max} \ll 26\,000\,\mathrm{V\,m^{-1}}$. According to the simulation, the highest value of the field in the region travelled by the beam is $1300\,\mathrm{V\,m^{-1}}$ for a voltage of 50 V applied to the lower plate. Letting the maximum electric field to be $13\,000\,\mathrm{V\,m^{-1}}$, the maximum accepted voltage is 500 V.

The data for two different measurements are reported in figure 4.1, together with the fit made using equation

$$I = A_i V^2 e^{-B_i V^2} + C_i \tag{4.2}$$

as done for the simulated data. Both measurements starting parameters are the same, but their amplitudes and offsets are different, showing the difficult control of the beam properties. These datasets provide a direct estimation of the sensitivity of the device: the electric field induced signal starts to be distinguishable from the background for $V = 20\,\mathrm{V}$, which correspond to an electric field of 4 V/cm between the plates (in the approximation of perfect capacitor). This can be considered the minimum electric field that can be detected with the EFILE diagnostic.

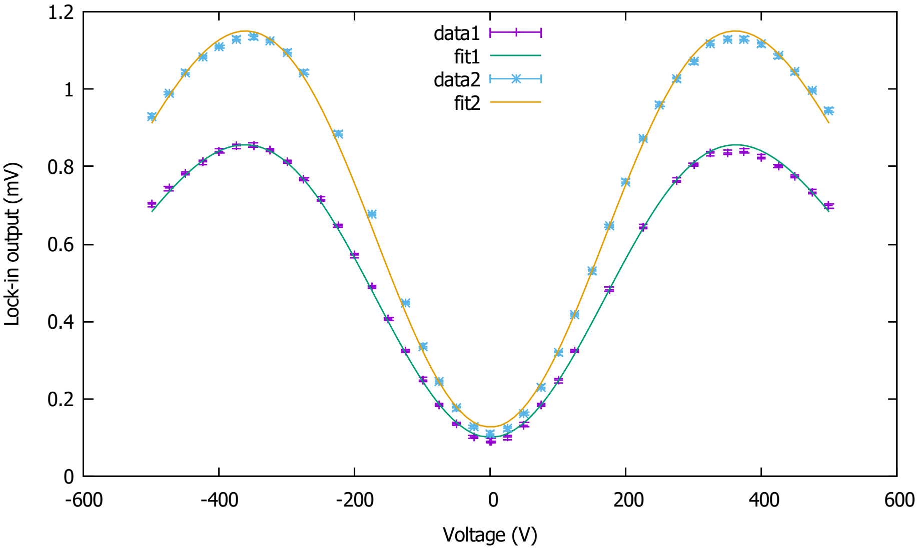

Figure 4.1: Lock-in output for different voltages applied to the lower plate with respect to the vessel.

Fit results are

$$\begin{aligned} A_1 &= (1.57 \pm 0.01) \times 10^{-5}\,\mathrm{mV/V^2} \\ B_1 &= (7.62 \pm 0.04) \times 10^{-6}\,\mathrm{V^{-2}} \\ C_1 &= (0.100 \pm 0.003) \times \mathrm{mV} \end{aligned}$$

for the first dataset and

$$\begin{aligned} A_2 &= (2.13 \pm 0.02) \times 10^{-5}\,\mathrm{mV/V^2} \\ B_2 &= (7.66 \pm 0.06) \times 10^{-6}\,\mathrm{V^{-2}} \\ C_2 &= (0.126 \pm 0.005) \times \mathrm{mV} \end{aligned}$$

for the second, and both datasets are well reproduced by the fits. The positions of the maxima are given by

$$\begin{aligned} V_{1,max} &= \sqrt{1/B_1} = (362 \pm 1)\,V \\ V_{2,max} &= \sqrt{1/B_2} = (361 \pm 1)\,V \end{aligned}$$

Although the two amplitudes (parameters A_1 and A_2) and offsets (parameters C_1 and C_2) are not compatible, the positions of the maxima (given by parameters B_1 and B_2) are comparable, showing that the shape of the curve only depends on the the electric field spatial distribution and is independent of the beam characteristics. Moreover, both fitting curves reproduce the experimental data quite well, showing that the simple model described in section 2.2 (which takes into account the edge effect of a real capacitor) works well for the static configuration used.

From fit results it is also possible to obtain the ratio $(z_0 - z_S)/(2\delta + 1)$, linked to the distance swept by the beam under the influence of the electric field:

$$\left(\frac{z_0 - z_S}{2\delta + 1}\right)_1 = (2.09 \pm 0.01)\text{cm} \quad ; \quad \left(\frac{z_0 - z_S}{2\delta + 1}\right)_2 = (2.10 \pm 0.02)\text{cm}$$

and the values are similar to the simulated one reported in 3.2. Assuming $z_0 - z_S \approx 10\,\text{cm}$ it gives $\delta \approx 1.8$.

4.1.1 Comparison with simulated results

The experimental data show the same behaviour as the simulated values reported in section 3.2. However, the values of B_1 and B_2 are not compatible with the simulated B' calculated in section 3.2. This is due to the parameters used for the simulation. To find the best parameters, both datasets were fitted with an adapted version of equation 2.8:

$$I = \beta \int_\Sigma n_{2s}(x, y, z_S) e^{-\int_{z_S}^{z_0} \gamma(\vec{E}) \frac{\mathrm{d}z}{v}} \left(1 - e^{-\int_{z_0}^{z_0+\Delta z} \gamma(\vec{E}) \frac{\mathrm{d}z}{v}}\right) \mathrm{d}x\mathrm{d}y + C \tag{4.3}$$

which was integrated using the electric field described in section 3.2.

The fitting parameters are β, C, z_0 and Δz, while z_S is fixed (it has been chosen such that $E(x, y, z_S) \approx 0$). The beam profile $n_{2s}(x, y, z_S)$ is a circle of $r = 10\,\text{mm}$ radius [18], and its value is set at $1/(\pi r^2)$ inside the circle and 0 outside. The integration area Σ is defined by the active surface of the photomultiplier: it is a rectangle of 8 mm height and 12 mm width. The integration along the vertical axis has been fixed to a 8 mm gap (from -4 mm to 4 mm), while the horizontal direction is linked to z_0 and Δz. The fit results are

$$\begin{aligned} z_{0,1} &= (-9.0 \pm 0.1)\,\text{mm} \\ (\Delta z)_1 &= (10.78 \pm 0.07)\,\text{mm} \\ \beta_1 &= (9.99 \pm 0.06)\,\text{mV} \\ C_1 &= (0.097 \pm 0.002)\,\text{mV} \end{aligned}$$

for the first set and

$$\begin{aligned} z_{0,2} &= (-9.95 \pm 0.09)\,\text{mm} \\ (\Delta z)_2 &= (13.53 \pm 0.09)\,\text{mm} \\ \beta_2 &= (10.96 \pm 0.06)\,\text{mV} \\ C_2 &= (0.118 \pm 0.002)\,\text{mV} \end{aligned}$$

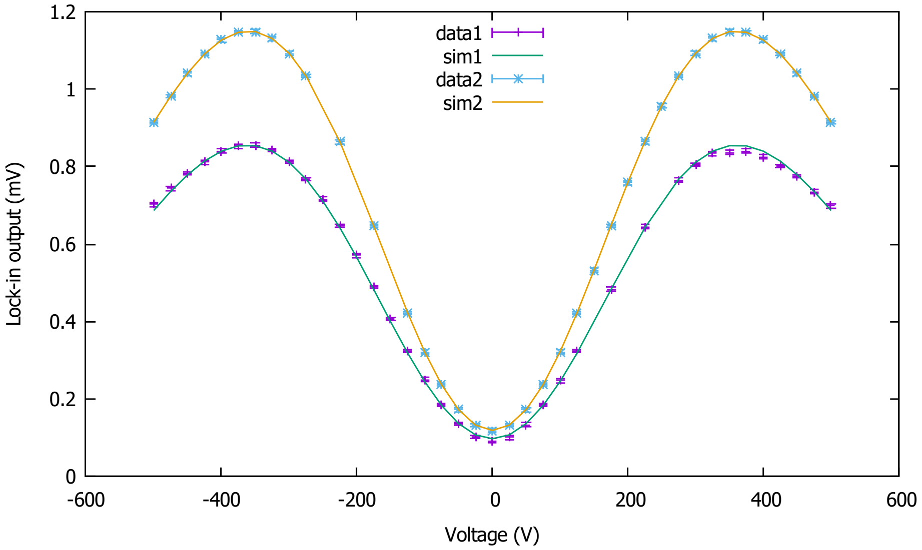

Figure 4.2: Comparison with the simulated output.

for the second one. Both fits are shown in figure 4.2.

As it can be seen, the newly simulated curves are adherent to the respective datasets, and both Δz are comparable with the expected width of the photomultiplier (12 mm), while the integration range along the z axis is shifted and it is not symmetric with respect to 0. The reason might be a misalignment of the photomultiplier with respect to the plates center (probably it is tilted of a few degrees), or it might be due to the different radial profile of the beam, that for fitting necessities was simply considered as a homogeneous circle of fixed diameter. However the measurements are well reproduced by the fitted simulations, which can therefore be used to represent the experimental data.

4.2 RF field

The static field measurements were used to calibrate the beam, and RF tests were performed after them. The lower plate was polarised with a radiofrequency signal with a frequency between $0.8 - 1.6\,\mathrm{GHz}$, and the RF generator connected to the amplifier could deliver a maximum power of $P_{max} = 33\,\mathrm{dBm} = 2\,\mathrm{W}$. In figure 4.3 the Lyman-α spectrum corresponding to the static dataset 2 described before is reported. The simulation described in section 3.3, calculated using the parameters determined with the fit procedure, is superposed. The shape of the peaks is not exactly reproduced:

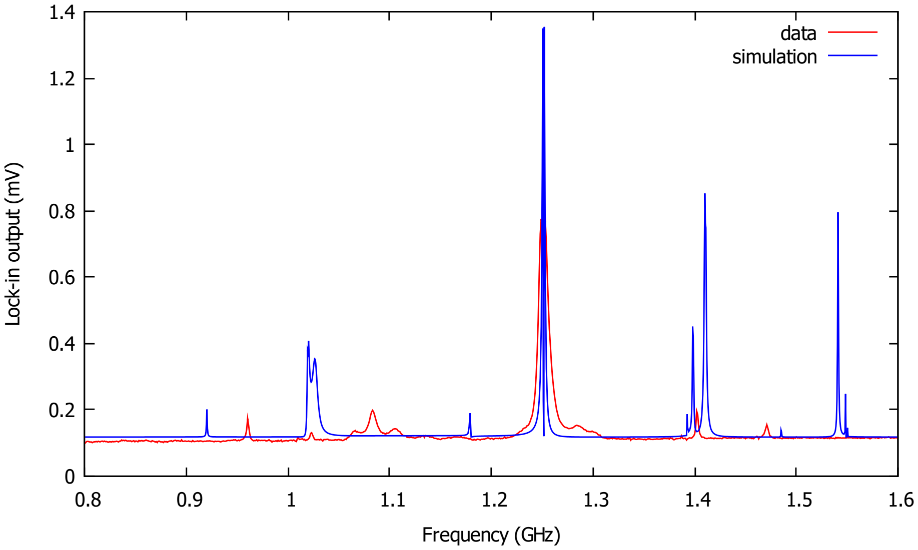

Figure 4.3: Comparison between the experimental and the simulated Lyman-α spectra.

the simulated peaks are higher and thinner than the experimental data. As said in section 3.3.2, this is due to the presence of losses in the transmission line, which broaden and lower the resonances and are not considered in the simulation.

Moreover, the experimental peaks are not placed at the same frequencies as the simulated ones, except for the peaks at 1.026 GHz, 1.252 GHz and at 1.400 GHz. This is probably due to the sensitivity of the resonant frequencies to geometrical details: figure 4.4 (a) shows the variations for vertical displacements of the plates, keeping the distance between them constant (5 cm), 4.4 (b) shows the variations for different distances between the plates. As it can be seen, the three peaks before mentioned are almost constant for the variations tested, explaining why they are found in both spectra.

Although the dynamical simulation can not reproduce the amplitude of the peaks, the eigenvalue simulation provides the shape of the electric field for the three frequencies for which a correspondence was found.

4.2.1 Estimation of the electric field

Several measurements for different injected powers were performed to study the behaviour of the emitted radiation at the frequencies of the three peaks. The measurements for the 1.026 GHz resonance could hardly be distinguished from the background, and therefore are not considered. The other two

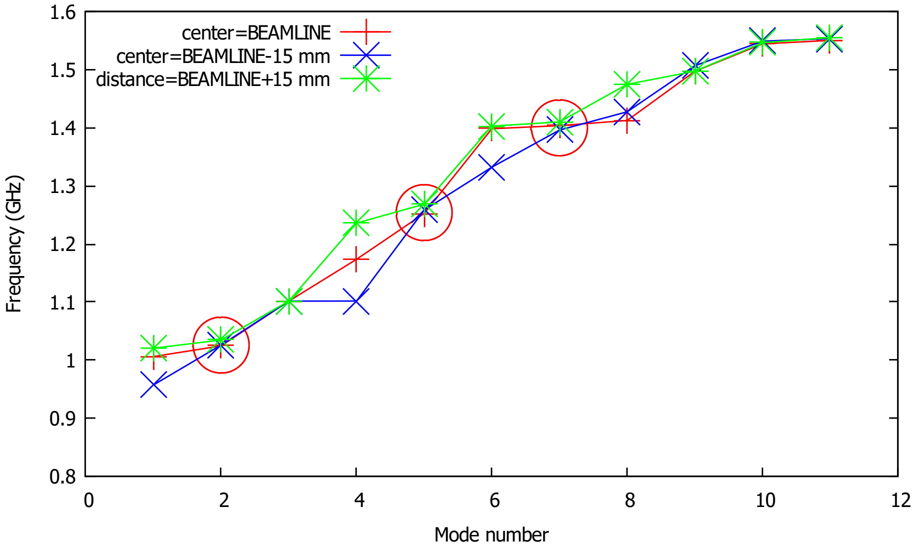

(a) *Same distance, vertical displacements.*

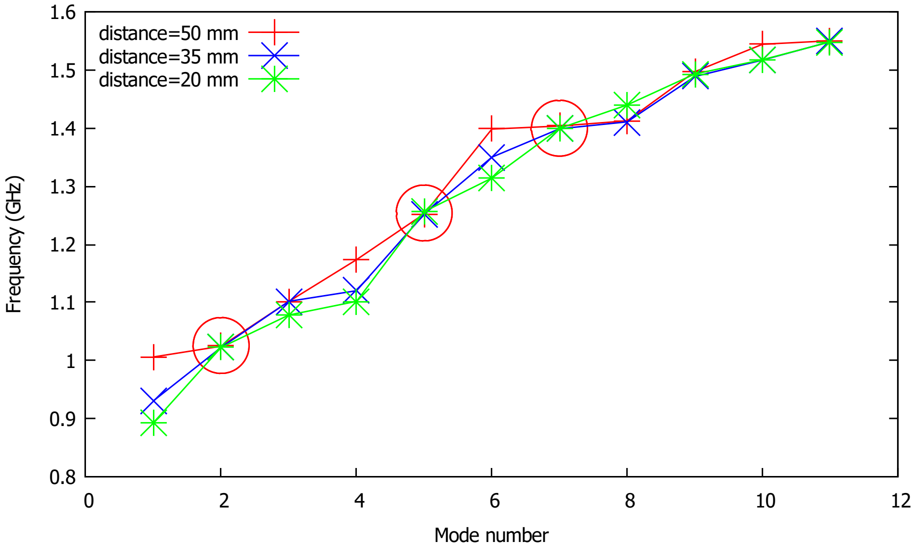

(b) *Same position, different distances.*

Figure 4.4: Variation of resonant frequencies for different positions of the plates. The peaks that are found in both the simulated and experimental RF spectra are highlighted.

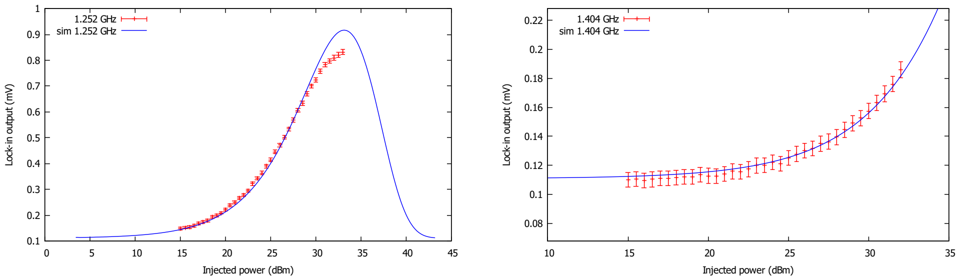

(a) 1.252 GHz *peak.* (b) 1.404 GHz *peak.*

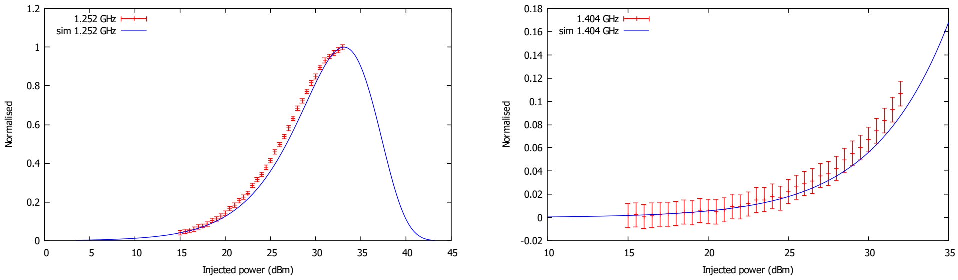

(c) 1.252 GHz *peak normalised.* (d) 1.404 GHz *peak normalised.*

Figure 4.5: Lyman-α measurements for different injected powers at fixed frequencies and comparison with the simulations.

datasets are presented in figure 4.5 (a) and (b), with the power emitted from the generator reported in dBm.

To compare the experimental data with the simulations, the field maps obtained with the eigenvalues simulation were used: as for the simulation of the Lyman-α signal with the static field described in section 3.2, the simulated electric field E_{eigen} was multiplied by different factors m and then equation 4.3 was integrated for every m, using the parameters determined in 3.2 for the static case fit. This way the expected behaviour of the signal was reproduced. Then the relation

$$P = \alpha E^2 \tag{4.4}$$

between power and electric field was used to superpose data and simulations, exploiting the property of logarithmic units such as dBm:

$$\begin{aligned} P[\mathrm{dBm}] = 10\log_{10}\left(\frac{\alpha m^2 E_{eigen}^2}{1\,\mathrm{mW}}\right) &= 20\log_{10}(m) \quad +10\log_{10}\left(\frac{\alpha E_{eigen}^2}{1\,\mathrm{mW}}\right) \\ &= 20\log_{10}(m) \quad +K \end{aligned}$$

where K is a constant. Therefore the abscissa of the experimental and simulated data only differ by a constant, which was determined by imposing the coincidence of one simulated and one experimental value.

As it can be seen, the data are well described by the simulation in the region before the saturation. Only the 1.252 GHz peak approaches the saturation, but at those values it moves away from the simulation. This is probably due to a variation of the beam properties with time, as these measurements were performed later than the one with static field. The values have then be normalized by subtracting the spontaneous emission constant and dividing by the highest value recorded for the 1.252 GHz case, and the results, reported in figure 4.5 (c) and (d), show a good agreement between simulation and experiment. Therefore, a correspondence between the simulated electric field and the Lyman-α radiation detected was found.

4.3 Rotated plates

To test the model with a different electric field configuration the plates were rotated by 90 degrees around the vertical axis (see figure 4.6), and the same measurements and analysis for static and oscillating voltage applied to the lower plate were performed for this set-up too.

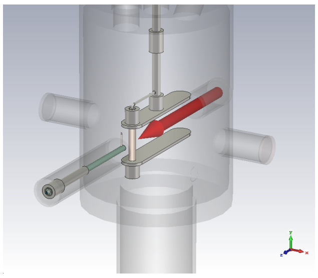

Figure 4.6: Model with the plates rotated by 90 degrees.

4.3.1 Static field

With this disposition the electric field is more intense and homogeneous along the beam path than before (for the almost cylindrical symmetry of the test chamber, the static field map is the same as reported in figure 3.3, with the z and x axis swapped). Therefore the saturation occurs at lower voltages, as shown in figure 4.7, together with the fitting curve of equation 4.2 and the simulation results. The results of the fits are

$$
\begin{aligned}
A &= (1.43 \pm 0.03) \times 10^{-5}\,\mathrm{mV/V^2} \\
B &= (2.48 \pm 0.04) \times 10^{-6}\,\mathrm{V^{-2}} \\
C &= (0.092 \pm 0.002) \times \mathrm{mV}
\end{aligned}
$$

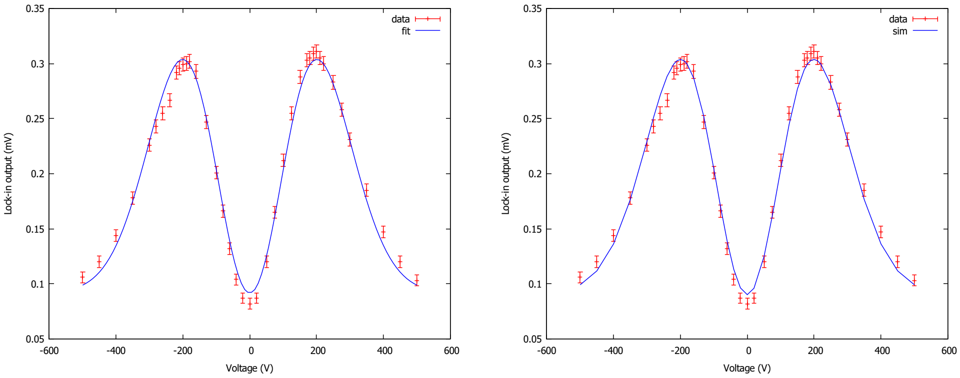

(a) *Comparison with equation 4.2.* (b) *Comparison with the simulation.*

Figure 4.7: measurements with static voltages, for the rotated plates configuration.

for the simple model and

$$\begin{aligned} z_0 &= (-1.5 \pm 0.5)\,\mathrm{mm} \\ \Delta z &= (11.4 \pm 0.2)\,\mathrm{mm} \\ \beta &= (8.0 \pm 0.1)\,\mathrm{mV} \\ C &= (0.090 \pm 0.001)\,\mathrm{mV} \end{aligned}$$

for the simulation. From B, the curve maxima are at

$$V_{max} = (201 \pm 2)\mathrm{V}$$

and

$$\left(\frac{z_0 - z_S}{2\delta + 1} \right) = (6.82 \pm 0.01)\mathrm{cm}$$

that, considering as before $z_0 - z_S \approx 10\,\mathrm{cm}$, gives $\delta \approx 0.2$. This result is smaller than the values found for the other configuration (around 1.6) and confirms that the field is more homogeneous along the beam line.

4.3.2 RF field

The resonant frequencies for the new configuration were determined with the resonant frequencies solver. The resulting eigenfrequencies are the same as the resonances of the previous configuration, as expected for the approximate cylindrical symmetry. The electric field maps of a few resonant frequencies are shown in figure 4.8, while the result of the frequency sweep for a fixed injected power in the range $0.8 - 1.5\,\mathrm{GHz}$ is presented in figure 4.9.

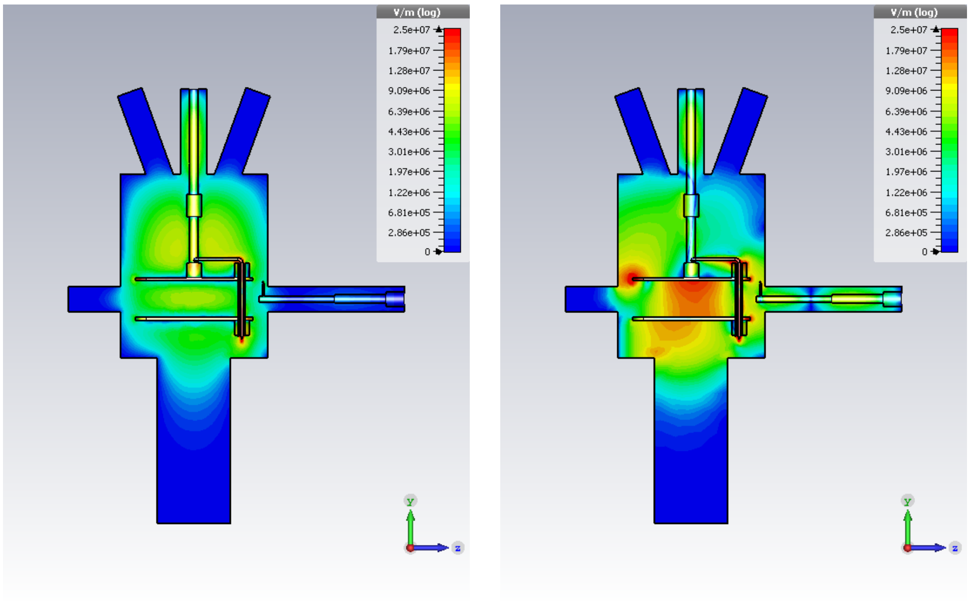

(a) 1.026 GHz (b) 1.252 GHz

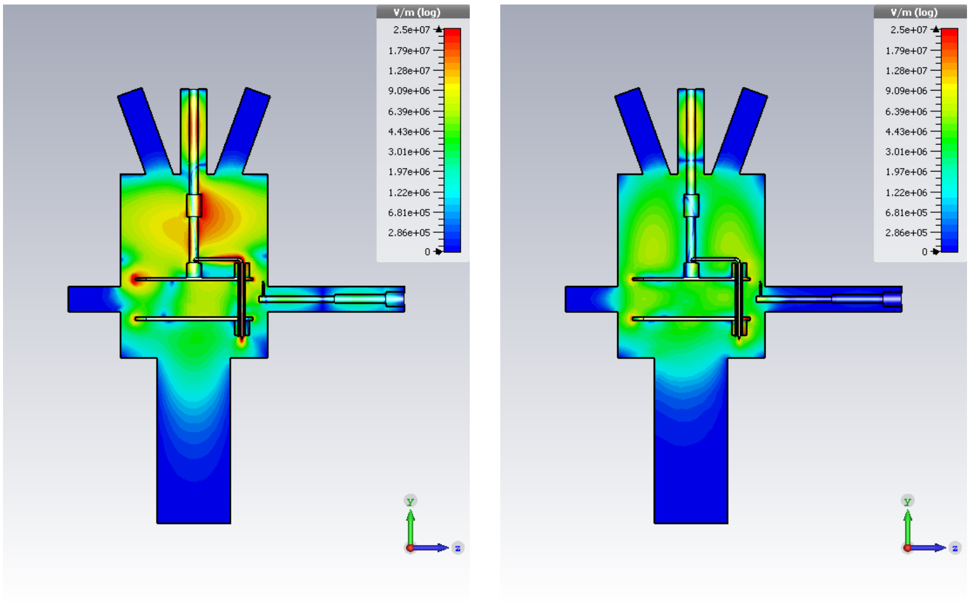

(c) 1.404 GHz (d) 1.550 GHz

Figure 4.8: Projections of the amplitude (in logarithmic scale) of the electric field on the plane perpendicular to the beam for various eigenvalues. The amplitude of the field is such that the entire energy stored in the electromagnetic field inside the vessel is 1 J.

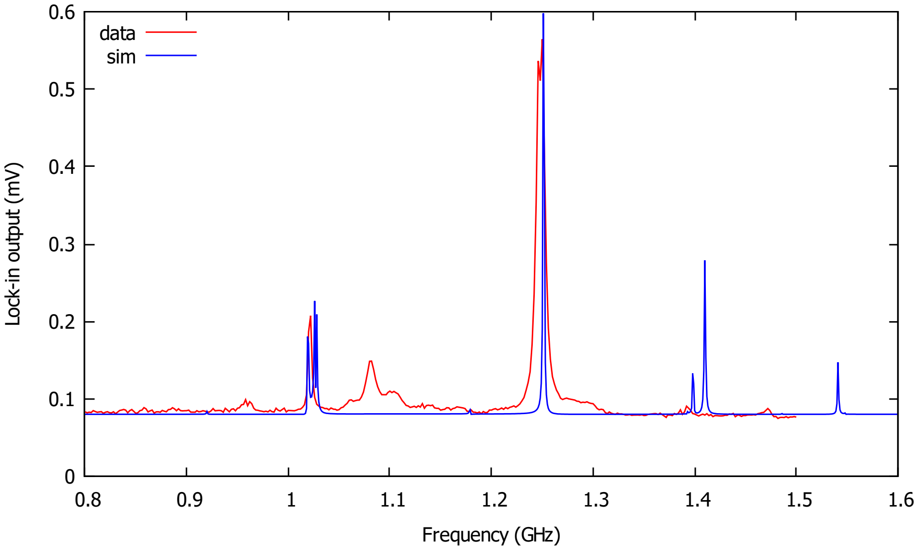

Figure 4.9: Lyman-α spectrum for the rotated plates model.

The peaks at 1.026 GHz, 1.252 GHz and 1.404 GHz are still present, but in this case it is the 1.404 GHz resonance that is hardly discernible from the background. Therefore only the power scans of the other two peaks are shown in figure 4.10, together with the respective simulated behaviour, superposed with the same method used for the previous configuration. After the normalisation the signal is well reproduced by the simulation.

Finally, the results presented in this chapter show that the model defined in chapter 2 reproduces the experimental data, confirming the dependence of the transition rate on the square of the magnitude of the electric field. However, it is not possible to state whether the transition rate given by expression 2.4 (which takes into account the hyperfine structure of the hydrogen atom) is correct or if it is possible to use equation 1.1 (which only considers the Lamb shift), since the frequencies analysed were too far from the resonances of the process for the two transition rates to be different enough. To investigate those resonances, the geometry of the test chamber needs to be changed, and a possible design implementation is presented in appendix C.

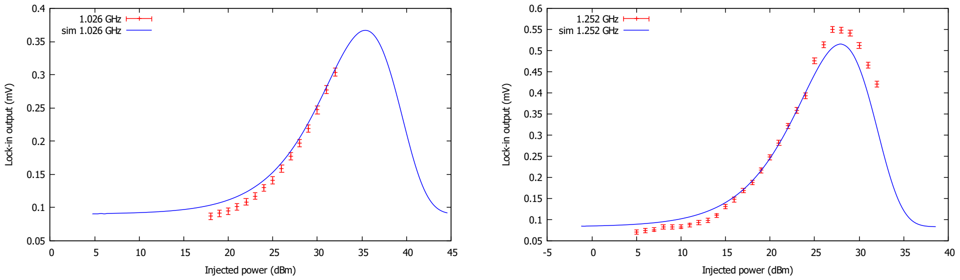

(a) 1.026 GHz *peak.* (b) 1.252 GHz *peak.*

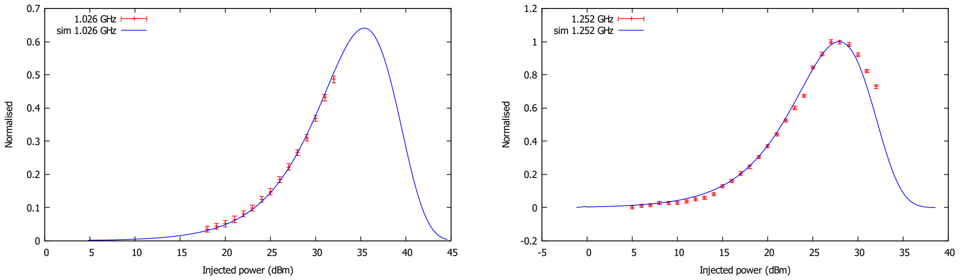

(c) 1.026 GHz *peak normalised.* (d) 1.252 GHz *peak normalised.*

Figure 4.10: Measurements as a function of the injected power at fixed frequencies and comparison with the simulation.

Chapter 5

Conclusions

This thesis focuses on the application of the EFILE diagnostic, currently installed at PIIM laboratory of Aix-Marseille Université. The aim of the device is to provide a tool for a non-intrusive measurement of the electric field in vacuum and in a plasma, such as in the edge region of a tokamak, using the Stark mixing between the $2s$ and $2p$ levels of a beam of neutral hydrogen prepared in the metastable $2s$ state. The rate of the process is proportional to the square of the magnitude of the electric field. Once in the $2p$ state, a hydrogen atom decays to the ground level, emitting Lyman-α radiation. The intensity detected with a photomultiplier therefore depends on the $2s \rightarrow 2p$ transition rate and consequently on the electric field.

Vacuum measurements were investigated by studying the response of the beam to a static or radio frequency electric field. From the expression of the transition rate, taking into account the hyperfine structure of the hydrogen atom, a model to interpret the experimental data was derived, showing that the light intensity emitted by the beam at a certain position strongly depends on the electric field encountered by the atoms during their flight. Finite element simulations of the electric field inside the test chamber were used to compare the model to the experimental data.

The static field simulations provided realistic field distributions and intensities, used to estimate the photomultiplier signal. Results were compatible with the experiments, and fits of the measurements were performed and used to get information on beam and measurement properties. The RF case instead could not be fitted: the real field magnitude, at a given frequency, for a given power delivered by the generator, was unknown because the apparatus was not properly adapted and the S-parameters were unknown too. However, the field maps of a few experimental resonant modes were calculated with the RF simulations, and estimations of the Lyman-α signal for the corresponding frequencies were obtained using the parameters of the static field fit. These results were superposed to the experimental data and presented the same behaviour.

This work confirms the dependence of the transition rate on the square of the magnitude of the electric field. It also gives a qualitative explanation in terms of resonant modes for the behaviour of the signal under radio frequency fields detected during previous experimental campaigns. Furthermore, it illustrates a direct association between experimental measurements and simulated electric fields.

5.1 Further developments

This thesis demonstrates that to get more than a qualitative result it is necessary to know the spatial distribution of the electric field in the region travelled by the beam. This can be obtained from electromagnetic simulations or by measuring at multiple positions along the beam line. The latter is preferable, because it allows to effectively measure an unknown electric field and because electromagnetic simulations strongly depend on the accuracy of the geometrical model. The frequency of the field is also needed, since the transition rate is not constant, and therefore the same signal intensity can be obtained by two fields of different magnitude and different frequency. Therefore, next step will be a better investigation of the transition rate behaviour near the resonant frequencies of the Stark mixing process, and a suggestion is reported in appendix C.

EFILE is planned to be used on two devices: the first one is MISTRAL, a magnetized plasma column installed at PIIM laboratory, aiming to measure the electric field of the plasma edge region. This will require the study of a new geometry for the machine, and further studies on the influence of the magnetic field. In MISTRAL, an argon magnetized plasma column is created with primary energetic electrons. Low frequency instabilities regularly rotating around this column are observed, and are well-described by the assumption that the electrons injected from the source exit radially from the central column and are subjected to the Lorentz force. This phenomenon could be addressed by directly measuring the electric field with EFILE [9].

The second test bench is ISHTAR, a RF antenna currently under development at IPP in Garching (Germany) for plasma heating. Here the shape of the electric field is given by accurate simulations, and the aim is to provide an absolute measurement of the electric field magnitude at one point. This configuration is similar to the one tested in this work.

Another open issue regards the calculation of the transition rate when two electric fields are present. In the plasma edge region there can be a superposition of electric fields of different frequency (for instance a static field and a travelling wave injected into the plasma). The transition rate for this configuration has not been calculated yet, and requires the study of a system like the one presented in equation B.30. One possible approach is the use of the density matrix technique [11].

Appendix A

Structure of the hydrogen atom

A.1 Fine structure

A one-electron atom can be described by the simple, non-relativistic Hamiltonian [2]

$$H_0 = \frac{p^2}{2m} + V(r) = \frac{p^2}{2m} - \frac{e^2}{(4\pi\epsilon_0)r} \tag{A.1}$$

which describes a particle (the electron) of mass m, elementary charge $-e$ and momentum operator p placed at a distance r from an infinite mass of charge e (the proton) located in the origin of the reference frame (ϵ_0 is the vacuum permittivity). The eigenvalues equation to be solved is

$$H\,|\psi_{nlm}\rangle = E_n\,|\psi_{nlm}\rangle \tag{A.2}$$

with $H = H_0$. The energy levels obtained from this Hamiltonian (the so called Bohr states) are

$$E_n = -\frac{1}{2n^2}\left(\frac{e^2}{4\pi\epsilon_0}\right)^2\frac{m}{\hbar^2} = -\frac{1}{2n^2}\,(a.u.) \tag{A.3}$$

with n the principal quantum number ($h = 2\pi\hbar$ is the Planck constant). Every energy level is $2n^2$ degenerate, and is in good agreement with experimental results, but the very precise measurements carried out in atomic physics require the addition of correction terms to H_0.

Instead of solving Dirac equation for a particle in a central potential, it is easier to use perturbation theory to write the new Hamiltonian as $H = H_0 + H'$, where H' contains the perturbative terms up to order v^2/c^2. The new energy levels are

$$E_{nj} = E_n\left[1 + \frac{\alpha^2}{n^2}\left(\frac{n}{j+1/2} - \frac{3}{4}\right)\right] \tag{A.4}$$

Table A.1: Comparison between Bohr levels and Dirac corrections.

State	E_n (eV)	ΔE_{Dirac} (eV)
$1s_{1/2}$	-13.6	-18.1×10^{-5}
$2s_{1/2}$	-3.40	-5.68×10^{-5}
$2p_{1/2}$	-3.40	-5.68×10^{-5}
$2p_{3/2}$	-3.40	-1.12×10^{-5}

where $\alpha \approx 1/137$ is the fine structure constant and a dependence on the total angular momentum quantum number $j = 1/2, ..., n - 1/2$ is introduced.

In table A.1 a comparison between the Bohr levels and the corresponding Dirac corrections for the hydrogen atom is reported. It is to be noted that the $2s_{1/2}$ and the $2p_{1/2}$ levels have the same energy.

In 1950 W. E. Lamb and R. C. Retherford [17] showed that the $2s_{1/2}$ actually lies higher than the $2p_{1/2}$ state, using microwave techniques to stimulate a direct *radio-frequency* transition between them. This discrepancy is due to QED radiative corrections related to interactions between the electron and electromagnetic fluctuations in vacuum, and its value is

$$\epsilon = 4.375 \times 10^{-6}\,\mathrm{eV} = 1058\,\mathrm{MHz} \cdot h$$

More precisely, the $2s_{1/2}$ state lies $4.301 \times 10^{-6}\,\mathrm{eV} = 1040\,\mathrm{MHz} \cdot h$ above the Dirac correction while the $2p_{1/2}$ lies $7.4 \times 10^{-8}\,\mathrm{eV} = 18\,\mathrm{MHz} \cdot h$ below.

A.2 Hyperfine structure

The next correction to the Hamiltonian A.1 arises from the magnetic interaction between the nucleus and the moving electron. Naming $\mathbf{I}$ the nuclear total angular momentum ($I = 1/2$ for the proton) and $\mathbf{F} = \mathbf{I} + \mathbf{J}$ the total angular momentum of the system, the correction for a state nl_j is

$$\Delta E = \frac{1}{2}\frac{m}{M_p} g_I \frac{\alpha^2}{n^3} \frac{F(F+1) - I(I+1) - j(j+1)}{j(j+1)(2l+1)} \, (a.u.) \qquad \text{(A.5)}$$

where M_p is the mass and $g_I = 5.5883$ is the Landé factor of the proton. The hyperfine splitting for the $n = 2$ is reported in table A.2 and a graphical resume of fine and hyperfine splitting is shown in figure A.1.

Table A.2: Energy differences from the Dirac and Lamb effects due to hyperfine splitting.

State	F	ΔE_{hyper} (eV)
$2s_{1/2}$	$F = 0$	-5.52×10^{-7}
	$F = 1$	1.84×10^{-7}
$2p_{1/2}$	$F = 0$	-1.84×10^{-7}
	$F = 1$	6.13×10^{-8}
$2p_{3/2}$	$F = 1$	-6.13×10^{-8}
	$F = 2$	3.68×10^{-8}

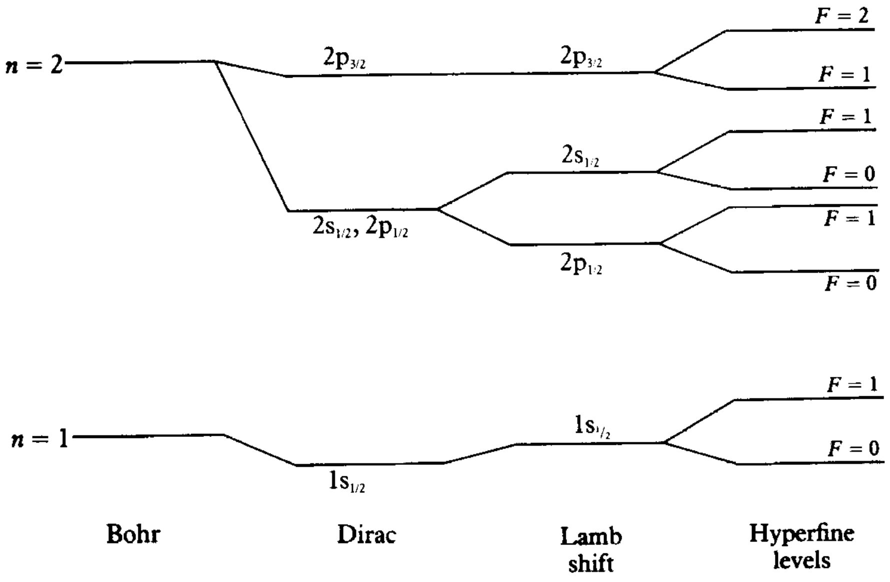

Figure A.1: Splitting of the $n = 1$ and $n = 2$ levels of hydrogen. The splitting is not to scale (picture taken from [2] page 264).

Appendix B

Derivation of the transition rate

The calculations presented in section B.1 are a resume of those presented in [27], [1] and [18], while those reported in section B.2 constitute a novel approach.

B.1 External perturbations

The time evolution of an isolated hydrogen atom is given, via the Schrödinger equation, by

$$|a,t\rangle = \sum_{\varphi} c_{\varphi}(t) e^{-iE_{\varphi}t/\hbar} |\varphi\rangle \tag{B.1}$$

where $\{E_{\varphi}\}$ is the complete set of energy levels associated to the $\{|\varphi\rangle\}$ eigenstates.

To describe the interaction of a $|a,t\rangle$ state with an external perturbation, a time dependent potential is added to the full Hamiltonian of the previous section:

$$H = H_0 + H' + V(t) \tag{B.2}$$

With this Hamiltonian, the time evolution of the coefficients $c_m(t)$ is given by [27]

$$i\hbar \frac{\mathrm{d}c_{\varphi}}{\mathrm{d}t} = \sum_{\psi} c_{\psi}(t) e^{-i\omega_{\varphi\psi}t} \langle\varphi| V(t) |\psi\rangle \tag{B.3}$$

where $\omega_{\varphi\psi} = (E_{\varphi} - E_{\psi})/\hbar$ is the resonant frequency.

The simplest kind of external perturbation is the interaction with the vacuum, which gives the probability of spontaneous emission. Let $|\varphi\rangle$ and $|\psi\rangle$ be two different eigenstates of the atomic hydrogen with $E_{\varphi} > E_{\psi}$. The probability of spontaneous emission from $|\varphi\rangle$ to $|\psi\rangle$ due to the interaction with the electromagnetic field is given, in the dipole approximation, by [26]

$$\Gamma^{spont}_{\varphi\psi} = \frac{\omega^3_{\varphi\psi} e^2}{3\pi\epsilon_0 \hbar c^3} |\langle\varphi| \mathbf{r} |\psi\rangle|^2 \tag{B.4}$$

where $\mathbf{r}$ is the position of the electron.

Assume the hydrogen atom can be in only two states: the metastable $2s_{1/2}$, as its lifetime is $0.14\,\mathrm{s}$ [18], and the $2p_{1/2}$, which has a lifetime $1/\Gamma = 1.59\,\mathrm{ns}$ [2] for the transition $2p_{1/2} \to 1s_{1/2}$. A time dependent perturbation applied to a two-states system can be described as [25]

$$V(t) = K_{12}(e^{i\omega t} |1\rangle \langle 2| + e^{-i\omega t} |2\rangle \langle 1|) \tag{B.5}$$

where K_{12} is a constant and ω is the oscillation frequency. Considering a perturbation in the form of a sinusoidally varying electric field in the z direction, the classical potential is

$$V(t) = -e\mathbf{E}(t) \cdot \mathbf{r} = -eE(t)z \tag{B.6}$$

and the time evolution of the system depends therefore on the value of $\langle\varphi| z |\psi\rangle$.

The expectation value of z between the aforementioned states depends on the magnetic quantum number l and m and is non-zero only when $\Delta l = \pm 1$ and $\Delta m = 0$. Let therefore be $|1\rangle = |2s_{1/2}\rangle$ and $|2\rangle = |2p_{1/2}, m = 0\rangle$. The calculation gives

$$\langle 1| z |2\rangle = -3a_0 = -1.59\,\text{Å} \tag{B.7}$$

where $a_0 = 0.53\,\text{Å}$ is the Bohr radius. The z operator can then be written as [27]

$$z = -3a_0(|1\rangle \langle 2| + |2\rangle \langle 1|) \tag{B.8}$$

and the electric field $E(t)$ as

$$E(t) = E_0(e^{-i\omega t} |1\rangle \langle 1| + e^{i\omega t} |2\rangle \langle 2|)$$

The set of equations B.3 for the two-state system is therefore given by (c_1 is associated to the $2s_{1/2}$ system and c_2 to the $2p_{1/2}$)

$$\begin{cases} \frac{\mathrm{d}c_1}{\mathrm{d}t} = -3i\left(\frac{a_0 e E_0}{\hbar}\right) e^{-i(\omega-\omega_{12})t} c_2 \\ \frac{\mathrm{d}c_2}{\mathrm{d}t} = -3i\left(\frac{a_0 e E_0}{\hbar}\right) e^{i(\omega-\omega_{12})t} c_1 - \frac{\Gamma}{2} c_2 \end{cases} \tag{B.9}$$

with the ansatz

$$\begin{cases} c_1(t) = e^{-\gamma t} \\ c_2(t) = \hat{c}_2(t) e^{-(\Gamma/2)t} \end{cases} \tag{B.10}$$

and the initial condition $c_1 = 1$, $c_2 = 0$ (pure $2s_{1/2}$ state). The $e^{-(\Gamma/2)t}$ takes into account the $2p_{1/2} \to 1s_{1/2}$ transition, and the use of $\Gamma/2$ instead of Γ stems from the fact that the transition rate is given for $|c_2|^2$. The solution is (see [18] and [27])

$$\gamma = \left(\frac{3a_0eE_0}{\hbar}\right)^2 \frac{1 - e^{-i(\omega-\omega_{12})t}e^{(\gamma-(\gamma/2))t}}{\Gamma/2 - \gamma + i(\omega - \omega_{12})} \approx \left(\frac{3a_0eE_0}{\hbar}\right)^2 \frac{\Gamma/2 - i(\omega - \omega_{12})}{(\Gamma/2)^2 + (\omega - \omega_{12})^2}$$

The last approximate equality is true in the weak field approximation, for which $\gamma \ll \Gamma/2$.

To get the overall exponential decay, the real part of γ has to be considered. Also, a factor of 2 comes in again because the relevant quantity is $|c_1|^2$. The transition rate is therefore given by:

$$\gamma = 9\left(\frac{a_0eE_0}{\hbar}\right)^2 \frac{\Gamma}{(\Gamma/2)^2 + (\omega - \omega_{12})^2} \tag{B.11}$$

However, experimentally it was found that the real transition rate is 1/3 of the expected γ. This is due to the fact that the entire $|2p\rangle$ state has to be considered, since it is given by a linear combination of the three states with $m = 0, \pm 1$, of which only the state with $m = 0$ has a non zero contribution to the calculation in B.7.

B.2 A different approach

A different calculation of the transition probability between the $|2p\rangle$ state ($\Gamma = 1/\tau_{2p} = 2\pi \cdot 100\,\mathrm{MHz}$) and the $|2s\rangle$ metastable state ($1/\tau_{2s} \approx 7\,\mathrm{s}^{-1} \approx 0$) of the hydrogen atom when a static electric field $\vec{\epsilon} = \epsilon\hat{z}$ is present is derived here. In the following, the index 1 is referred to the $|2p\rangle$ state, while index 2 is used for the $|2s\rangle$. The formalism used is the same as in chapter 4 of [5].

Let the system be made of only the two states $|1\rangle$ and $|2\rangle$. In this basis, the Hamiltonian in the absence of the electric perturbation is

$$H_0 = \begin{pmatrix} E_1 - i\hbar\Gamma & 0 \\ 0 & E_2 \end{pmatrix} \tag{B.12}$$

and the imaginary part of the eigenvalue associated to $|1\rangle$ takes into account the finite lifetime of the state.

The electrical perturbation can be written classically as $W = -e\vec{r} \cdot \vec{\epsilon} = -ez\epsilon$, where e is the electron charge, $\vec{r}$ is its distance from the nucleus and therefore $-e\vec{r}$ is the electric dipole of the electron. As

$$\langle i|\, z\, |j\rangle = -3a_0(1 - \delta_{ij})$$

where a_0 is the Bohr radius, the quantum mechanic representation of the perturbation H_1 is the anti-diagonal matrix

$$H_1 = \begin{pmatrix} 0 & W \\ W & 0 \end{pmatrix} \tag{B.13}$$

where $W = 3a_0eE$.

B.2.1 Diagonalisation of the Hamiltonian

The perturbed Hamiltonian $H = H_0 + H_1$ has new eigenvalues:

$$\epsilon'_{1,2} = \frac{\epsilon_1 + \epsilon_2}{2} - i\hbar\frac{\Gamma}{4} \mp \frac{1}{2}\sqrt{C^2 + 4W^2} \tag{B.14}$$

where $C = (\epsilon_2 - \epsilon_1) + i\hbar\frac{\Gamma}{2}$. Assuming $|W| \ll \sqrt{(\epsilon_2 - \epsilon_1)^2 + \hbar^2\frac{\Gamma^2}{4}} \approx \epsilon_2 - \epsilon_1$, which means $E \ll 2.6 \times 10^4\,\mathrm{V/m}$, equation B.14 gives

$$\epsilon'_1 \approx \epsilon_1 - i\hbar\frac{\Gamma}{2} - \frac{W^2}{\epsilon_2 - \epsilon_1 + i\hbar\frac{\Gamma}{2}} \tag{B.15}$$

$$\epsilon'_2 \approx \epsilon_2 + \frac{W^2}{\epsilon_2 - \epsilon_1 + i\hbar\frac{\Gamma}{2}} \tag{B.16}$$

The eigenvectors are given by $(H - \epsilon'_j\mathbb{1})(x\,|1\rangle + y\,|2\rangle) = 0$. With the same approximation, they are:

$$|\psi_1\rangle = |1\rangle - \frac{W}{C}\,|2\rangle \tag{B.17}$$

and

$$|\psi_2\rangle = \frac{W}{C}\,|1\rangle + |2\rangle \tag{B.18}$$

$\{|\psi_1\rangle, |\psi_2\rangle\}$ is the new basis in which the H matrix is diagonal. The change of basis matrix is

$$M = \begin{pmatrix} 1 & \frac{W}{C} \\ -\frac{W}{C} & 1 \end{pmatrix} \tag{B.19}$$

with inverse

$$M^{-1} = \begin{pmatrix} 1 & -\frac{W}{C} \\ \frac{W}{C} & 1 \end{pmatrix} \tag{B.20}$$

where $C^2 \approx |C|^2 \gg W^2$ was assumed.

B.2.2 Time evolution and transition probability

Let $\{|\psi_j\rangle\}$ be the basis of a system with a time independent Hamiltonian H. The system at time $t = 0$ is in the state $|\psi(0)\rangle = \sum_j a_j |\psi_j\rangle$, where the a_j are complex constants. The evolution of the system is then given by

$$|\psi(t)\rangle = \sum_j a_j \exp(-i\frac{\epsilon_j}{\hbar}t)\,|\psi_j\rangle \tag{B.21}$$

where the ϵ_j are the eigenvalues of H.

The electron is assumed to be in state $|2\rangle = |\psi_2\rangle - \frac{W}{C}|\psi_1\rangle$ at time $t = 0$. Then the time evolution is given by

$$|\psi(t)\rangle = e^{-i\frac{\epsilon_2'}{\hbar}t}\,|\psi_2\rangle - \frac{W}{C}e^{-i\frac{\epsilon_1'}{\hbar}t}\,|\psi_1\rangle \tag{B.22}$$

where $C = \epsilon_2 - \epsilon_1 + i\hbar\frac{\Gamma}{2}$.

The probability to find the electron in state $|2\rangle$ at time t is then given by

$$\mathcal{P}_{2\to 2}(t) = |\,\langle 2|\psi(t)\rangle\,|^2 = |e^{-i\frac{\epsilon_2'}{\hbar}t} + e^{-i\frac{\epsilon_1'}{\hbar}t}\frac{W^2}{C^2}|^2 \tag{B.23}$$

$$\approx |e^{-i\frac{\epsilon_2'}{\hbar}t}|^2 = \exp(-\frac{W^2}{|C|^2}\Gamma t) = e^{-\gamma t} \tag{B.24}$$

with $\gamma = (3a_0E)^2\frac{\Gamma}{(\epsilon_2-\epsilon_1)^2+\hbar^2\frac{\Gamma^2}{4}}$ (same result obtained with the time dependent approach for the static case).

Similarly it is possible to calculate the probability to find the electron in state $|1\rangle$ at time t:

$$\mathcal{P}_{2\to 1}(t) = \frac{W^2}{|C|^2}[e^{-\frac{W^2}{|C|^2}\Gamma t} + e^{-\Gamma t(1-\frac{W^2}{|C|^2})} - 2e^{-\frac{\Gamma}{2}t}\cos(\frac{\epsilon_2-\epsilon_1}{\hbar}t)] \tag{B.25}$$

$$\approx \frac{W^2}{|C|^2}[1 + e^{-\Gamma t} - 2e^{-\frac{\Gamma}{2}t}\cos(\frac{\epsilon_2-\epsilon_1}{\hbar}t)] \tag{B.26}$$

As it is proportional to $\frac{W^2}{|C|^2}$, it is negligible. This means that if the electron passes from state 2 to state 1, then it almost instantly decays to the ground state.

B.2.3 Adding a time dependent perturbation

A time dependent electric field along the z axis can be classically written as

$$E(t) = E_0e^{-i\omega t} \tag{B.27}$$

and the corresponding Hamiltonian for the original system can be written as

$$H(t) = \begin{pmatrix} 0 & V(t) \\ V^*(t) & 0 \end{pmatrix} = \begin{pmatrix} 0 & 3a_0eE_0e^{-i(\omega-\omega_{12})t} \\ 3a_0eE_0e^{i(\omega-\omega_{12})t} & 0 \end{pmatrix} \tag{B.28}$$

where $\omega_{12} = \frac{\epsilon_2-\epsilon_1}{\hbar}$. This matrix has to be transformed in the new system with basis $\{|\psi_1\rangle, |\psi_2\rangle\}$. The new matrix is

$$H'(t) = M^{-1}H(t)M \approx \begin{pmatrix} -\frac{W}{C}(V(t)+V^*(t)) & V(t) \\ V^*(t) & \frac{W}{C}(V(t)+V^*(t)) \end{pmatrix} \tag{B.29}$$

This matrix leads to a system of differential equation to describe the time evolution of the state $|\psi(t)\rangle = b_1(t)|\psi_1\rangle + b_2(t)|\psi_2\rangle$:

$$\begin{cases} i\hbar\frac{\mathrm{d}b_1}{\mathrm{d}t} &= -\frac{W}{C}(V(t)+V^*(t))b_1 + V(t)b_2 \\ i\hbar\frac{\mathrm{d}b_2}{\mathrm{d}t} &= +\frac{W}{C}(V(t)+V^*(t))b_2 + V^*(t)b_2 \end{cases} \tag{B.30}$$

Appendix C

Geometry improvement

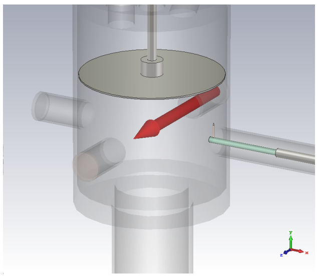

Figure C.1: The new geometry proposed.

Chapter 4 shows that the measurements performed with the EFILE diagnostic can be related to field maps obtained from finite element simulations, allowing a calibration of the diagnostic for the static field case and for a few frequencies. However, the resonant behaviour around the resonant frequencies of the $2s \rightarrow 2p$ transition could not be tested: a signal differing from the background could indeed be detected between 1.05 GHz and 1.15 GHz (see both figures 4.3 and 4.9), but a correspondence with the simulated Lyman-α spectrum could not be found. This is probably due to the complex geometry of the interior of the vessel, which is hard to simulate and produces a lot of different resonant electric fields. Moreover, the intensity of the peaks could not be properly reproduced, since the simulation did not take into account signal losses along the transmission line. Resonances are nevertheless needed, because otherwise no signal would be detected.

The design of the test chamber was therefore simplified, allowing an easier control of the cavity eigenfrequencies. The idea is to excite eigenmodes similar to the cylindrical TM and TE modes described in section 3.3.1. To do so, the plates were substituted with a disc (called *piston*, see figure C.1) having a slightly smaller diameter than the vessel (195 mm). It can be placed at different heights (h) from the bottom of the main cylinder. By modifying the distance h between the bottom of the main cylinder and the piston, the eigenfrequencies can be varied, allowing a scan of the resonance behaviour of the Stark mixing. The stimulation of the RF field is made by polarising the probe shown in figure 3.1 (c). The Lyman-α spectra acquired for three different h (for an injected power of 33 dBm) and the measurements of the

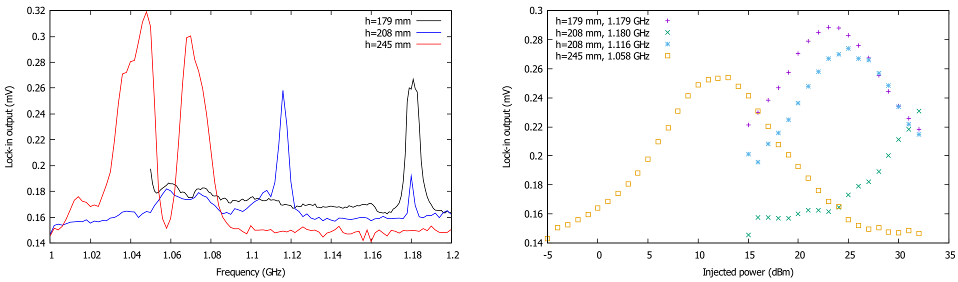

(a) *Lyman-α spectra for different h, with* 33 dBm *injected power.*

(b) *Measurements of the peaks for different injected powers.*

Figure C.2: Measurements as a function of the injected power at fixed frequencies and comparison with the simulation.

Table C.1: Eigenfrequencies for different h.

h	Experimental (GHz)	Simulation (GHz)	Mode
179 mm	1.179	1.182	TM
208 mm	1.180	1.177	TM
	1.116	1.121	TE
245 mm	1.058	1.058	TE

peaks for different injected powers are shown in figure C.2. The positions of the peaks, together with the simulated correspondent eigenvalues and the mode type are reported in table C.1

As it can be seen, all the peak frequencies present in the experimental spectra are reproduced by the simulation within a few MHz (the spectra for $h = 245$ mm does not present two peaks, but only one, which is saturated). Furthermore, the spectra show that the position of the peaks can be controlled by changing the height h, obtaining cavity eigenmodes near the resonant frequencies of the Stark mixing process. However, the results presented in figure C.2 (b) can not be interpreted as done for the other configuration, because at present it is not possible to perform static field measurements which would allow the determination of the simulation parameters z_0, Δz, β and C.

Bibliography

[1] J. F. Benage. 'Plasma effects on the metastable $H^0(2s)$ atom'. PhD thesis. University of Colorado, Boulder, CO, 1986.

[2] B. H. Bransden and C. J. Joachain. *Physics of Atoms and Molecules, 2nd edition.* Ed. by Prentice Hall. 2003.

[3] F. F. Chen. *Introduction to Plasma Physics and Controlled Fusion.* Ed. by Springer. 1984.

[4] L. Chérigier-Kovacic et al. 'Electric field induced Lyman-α emission of a hydrogen beam for electric field measurements'. In: *Review of Scientific Instruments* 86 (2015), p. 063504.

[5] C. Cohen-Tannoudji, B. Diu, and F. Laloë. *Mécanique quantique.* Ed. by Hermann. 1977.

[6] C. Cohen-Tannoudji and D. Guéry-Odelin. *Advances in Atomic Physics: an Overview.* Ed. by World Scientific Publishing. 2011.

[7] *CST - Computer Simulation Technology.* URL: `www.cst.com`.

[8] F. Doveil, A. Lejeune, and L. Chérigier-Kovacic. 'Lyman-α radiation of a probing metastable hydrogen beam to measure electric fields in diluted fluids and plasmas'. In: *Physics of Plasmas* 20 (2013), p. 055701.

[9] A. Escarguel. 'Optical diagnostics of a low frequency instability rotating around a magnetized plasma column'. In: *The European Physical Journal D* 56 (2010), pp. 209–214.

[10] R. P. Feynman, M. L. Sands, and Leighton R. B. *The Feynman Lectures on Physics.* Ed. by Addison-Wesley. 1964.

[11] G. Grynberg and C. Fabre. *Introduction aux lasers et à l'optique quantique.* Ed. by Ellipses. 1997.

[12] T. Guillaume. *Mesures de champ électrique par le diagnostic EFILE.* M2 Report. Aix-Marseille Université, 2017.

[13] T. Guillaume. *Mesures électriques et optiques d'un champ radiofréquence.* M1 Report. Aix-Marseille Université, 2016.

[14] G. Herzberg. *Atomic Spectra and Atomic Structure.* Ed. by Dover Publications. 1944.

[15] J. Jin. *The Finite Element Method in Electromagnetics, 2nd edition.* Ed. by John Wiley and Sons. 2002.

[16] M. Kikuchi, K. Lackner, and Q. M. Tran, eds. *Fusion Physics.* IAEA International Atomic Energy Agency, 2012.

[17] W. E. Lamb and R. C. Retherford. 'Fine structure of the hydrogen atom'. In: *Physical Review Letters* 79.4 (1950), pp. 549–572.

[18] A. Lejeune. 'Mise au point d'un diagnostic optique non-intrusif pour la mesure des microfluctuations locales des champs électriques dans les plasmas'. PhD thesis. Turbulence Plasma, PIIM, Aix-Marseille Université, 2010.

[19] A. Lejeune, L. Chérigier-Kovacic, and F. Doveil. 'Innovative measurement of Debye shielding in plasmas by Lyman-α radiation of a probing metastable hydrogen beam'. In: *AIP Conference Proceedings* 1582 (2014), pp. 261–268.

[20] S. R. Lundeen, P. E. Jessop, and F. M. Pipkin. 'Measurement of the Hyperfine Structure of $2^2P_{1/2}$ State in Hydrogen'. In: *Physical Review Letters* 34.7 (1975), pp. 377–380.

[21] E. Martines. 'Corso di Fisica della fusione nucleare e applicazioni dei plasmi. Parte I: Fisica della fusione nucleare'. Università degli Studi di Padova. A. A. 2016-2017.

[22] E. Matricciani. 'Introduzione ai circuiti a microonde (circuiti passivi)'. Università degli Studi di Padova. 1989.

[23] L. Pauling and S. Goudsmit. *The Structure of Line Spectra.* Ed. by McGraw-Hill. 1930.

[24] P. Pradel. 'Formation of H(n = 2) atoms by the nearly resonant process H^+ in Cs. Multiple collision processes'. In: *Physical Review A* 10.3 (1974), pp. 797–812.

[25] J. J. Sakurai and J. Napolitano. *Modern Quantum Mechanics, 2nd edition.* Ed. by Pearson. 2011.

[26] L. Salasnich. *Quantum Physics of Light and Matter.* Ed. by Springer. 2014.

[27] P. Ström. 'Measurements of electric fields in a plasma by Stark mixing induced Lyman-α radiation'. Master thesis. Aix-Marseille Université, 2013.

[28] M. Vallar. *Measurement of a radio frequency electric Field by Lyman-α emission of a metastable hydrogen atomic beam.* M1 Report. Aix-Marseille Université, 2014.

[29] H. White. *Introduction to Atomic Spectra.* Ed. by McGraw-Hill. 1934.

[30] A. Wolski. 'Theory of electromagnetic fields'. In: *Proceedings of the CAS-CERN Accelerator School: RF for accelerators.* Ed. by R. Bailey. CERN-2011-007, 8-17 June 2010, pp. 15–66.

Remerciements

Mon travail de thèse n'aurait pas été possible sans l'aide de beaucoup de personnes. D'abord je remercie Laurence Chérigier-Kovacic pour avoir accepté d'être mon maître de stage et m'avoir guidé dans mon travail; Fabrice Doveil et Yves Elskens pour les nombreuses et fructueuses discussions; tous les membres de l'équipe Turbulence Plasma du laboratoire PIIM pour m'avoir accueilli entre eux; Guillaume Demesy, Pierre Sabouroux et Marc Dubois de l'institut Fresnel, pour la licence de CST et l'aide avec les simulations; Théo Guillaume, collègue de Master qui a travaillé avec moi sur le même appareil, en se concentrant surtout sur la partie de l'acquisition des données expérimentales. Je remercie en outre mon superviseur de Padoue Gianluigi Serianni, pour ses suggestions et son activité de "correcteur des épreuves". Enfin je remercie mes parents, qui m'ont permis d'arriver jusqu'ici et m'ont toujours soutenu.